Investigating Chamber-Dependent Cardiac Remodelling in a Murine Model of Heart Failure with Preserved Ejection Fraction

Christian Barakat

A thesis submitted to the Faculty of Graduate Studies in partial fulfillment of the requirements for the degree of Master of Science

Department of Biology
York University
Toronto, Ontario

December 2025

Abstract

Heart failure with preserved ejection fraction (HFpEF) is strongly associated with atrial fibrillation (AF), yet chamber-specific mechanisms remain poorly defined. This thesis characterizes a HFpEF model using high-fat diet, sucrose, and L-NAME (HFDLS), a combination that has not been explored in the CD1 mouse strain.

Relative to normal-diet controls, HFDLS mice showed greater percent body-weight gain (45.9 to 70.8%), reduced exercise tolerance (408 to 276 m), and elevated mean arterial pressure (84.7 to 107.6 mmHg). Invasive hemodynamics demonstrated increased LV end-diastolic pressure (6.7 to 11.8 mmHg), consistent with impaired diastolic filling. Echocardiography confirmed preserved ejection fraction with concentric remodeling. Histological analysis revealed increased fibrosis in the left atrium (5.96 to 12.15%) and left ventricle (1.71 to 3.76%). Intracardiac electrophysiology showed signficantly prolonged atrial arrhythmia duration (2.6 to 23.6 s), with unchanged ventricular refractoriness. $F4/80^{+}$ immunostaining demonstrated increased macrophage density in both chambers.

Overall, the model produced a modest HFpEF phenotype that will require further refinement to strengthen disease severity, but it nevertheless revealed clear atrial-dominant structural and electrical remodeling, establishing a platform to investigate TNFα-mediated mechanisms linking HFpEF and AF.

Keywords: Heart Failure with Preserved Ejection Fraction, Atrial Fibrillation, CD1 mouse strain, High-Fat diet+L-NAME+Sucrose

Acknowledgements

I would like to begin by expressing my sincere appreciation to Dr. Peter Backx for his mentorship, patience, and constant guidance throughout my degree. His support pushed me to think more critically and approach science with greater discipline and confidence. I am grateful for the opportunity to work and learn under his supervision.

I also thank my committee members, Dr. Ali Abdul-Sater and Dr. Christopher Perry, for their thoughtful feedback, encouragement, and direction, which strengthened this project at every stage.

My gratitude extends to Dr. Robert Lakin, who performed the intracardiac electrophysiology assessment for this thesis and who always took the time to answer my conceptual and technical questions. His clear explanations and honest guidance kept my expectations grounded and helped me approach the work with confidence. I am equally thankful to Parashar Bhatt and Dana Sherrard for their guidance and training throughout my degree. I would also like to acknowledge the Backx laboratory team for creating a supportive and collaborative environment that made this experience both productive and enjoyable.

To my partner Arliese Garside, thank you for your constant encouragement, patience, and support. To my family and close friends, your belief in me has carried me through every part of this journey, and I am deeply grateful. Lastly, to Moush Moush and Maisie, thank you for being the best company through the long days and nights of writing and experiments.

Table of Contents

Abbreviations

AERP: Atrial effective refractory period
AF: Atrial fibrillation
AMPK: AMP-activated protein kinase
AUC: Area under the curve
AVERP: Atrioventricular effective refractory period
Cx40: Connexin-40
Cx43: Connexin-43
CnV: Conduction velocity
CO: Cardiac output
DBP: Diastolic blood pressure
EDP: End-diastolic pressure
EF: Ejection fraction
ERP: Effective refractory period
ESP: End-systolic pressure
FS: Fractional Shortening
GTT: Glucose tolerance test
HFD: High-fat diet
HFpEF: Heart failure with preserved ejection fraction
HFrEF: Heart failure with reduced ejection fraction
IL-6: Interleukin-6
IPGTT: Intraperitoneal glucose tolerance test
LA: Left atrium
L-NAME: Nω-Nitro-L-arginine methyl ester
LV: Left ventricle
LVEDP: Left ventricular end-diastolic pressure
MAP: Mean arterial pressure
NO: Nitric oxide
PBS: Phosphate-buffered saline
PSR: Picrosirius red
ROS: Reactive oxygen species
RV: Right ventricle
SA: Sinoatrial node
SBP: Systolic blood pressure
SERCA: Sarcoplasmic reticulum calcium ATPase
SK2: Small-conductance calcium-activated potassium channel 2
SR: Sarcoplasmic reticulum
SV: Stroke volume
TGF-β: Transforming growth factor Beta
TNFα: Tumor necrosis factor alpha
TPR: Total peripheral resistance
VERP: Ventricular effective refractory period

Figures and Tables List

Chapter 1: Introduction

1.1 Atrial Fibrillation and Heart Failure with Preserved Ejection Fraction

Atrial fibrillation (AF) and heart failure (HF) are the only two major cardiovascular conditions that are on the rise in the United States, both posing significant public health challenges[1]. Roughly half of all patients with heart failure have preserved ejection fraction (HFpEF), with HFpEF elicited by metabolic alterations emerging as the most prevalent form[1,2]. HFpEF differs from HF with reduced ejection fraction (HFrEF) in that EF is greater than or equal to 50%, while in HFrEF, EF is less than or equal to 40%[3]. Studies have found that approximately two-thirds of patients with HFpEF are likely to develop AF as their condition progresses[2].

AF is the most common arrhythmia in clinical practice, with incidence and prevalence increasing globally, projected to reach up to 16 million individuals in the US by 2050[4]. AF manifests as a rapid and irregular stimulation of the atria, leading to dyssynchronous atrial contraction and erratic excitation of the ventricles, which in turn diminishes cardiac output, restricts blood flow, and increases the risk of stroke[5,6] The incidence of this arrhythmia is significantly increased in patients with cardiovascular diseases (valvular disease and heart failure (HFpEF and HFrEF)) and in patients with conditions linked to poor cardiovascular health (hypertension, diabetes, and obesity), which are associated with increasing age[7,8].

A common link with ageing and poor cardiovascular health is elevated diastolic filling, leading to increased pressure and stretch, which stimulates many signalling pathways linked to hypertrophy, fibrosis, and inflammation[9]. Currently, there are limited proven effective medical therapies for HFpEF and AF; thus, further research is needed to elucidate the underlying mechanisms of these diseases[1,10]. To investigate the mechanisms underlying AF development in the context of HFpEF, this study employs a murine model combining a high-fat diet (HFD), the nitric oxide synthase inhibitor Nω-Nitro-L-arginine methyl ester (L-NAME), and sucrose supplementation.

Understanding how atrial remodelling, electrophysiological alterations, and systemic comorbidities interact is crucial to explaining the mechanisms by which patients with HFpEF are

predisposed to AF. The following sections outline the structural and electrical foundations that underlie these processes.

1.2 Fundamentals of Cardiac Structure and Electrophysiology

The heart is a muscular pump consisting of four chambers that contract in a coordinated manner, which maintains pulmonary and systemic circulation[11]. Deoxygenated blood from the systemic circulation enters the right atrium and flows into the right ventricle, which then pumps the blood into the pulmonary circulation, where it is oxygenated. The oxygenated blood then enters the left atrium, passes into the left ventricle, which then forcefully ejects it through the aorta to the systemic circulation. Unidirectional flow is maintained via the atrioventricular and semilunar valves, which open and close with pressure changes during the cardiac cycle. The atria contribute to ventricular filling through three distinct mechanical phases[12]. During ventricular systole, the atrioventricular valves are closed, and the atria collect blood from the systemic and pulmonary circulation, referred to as the reservoir phase[12]. During early diastole, when the ventricles are relaxed, the pressure in the ventricles drops and the atrioventricular valve opens, allowing blood to flow passively into the ventricles, which is referred to as the conduit phase[12]. During late diastole, the atria contract actively and, under normal conditions, contribute to 20-30% of ventricular filling volume, which is referred to as the atrial kick or booster pump phase[12,13]. This atrial kick becomes especially important when ventricular relaxation is impaired, which occurs with HFpEF.

Electrical impulses, known as action potentials (APs), originating from the sinoatrial node (SA), located in the right atrium, ensure that the contraction of the heart occurs in a tightly coordinated sequence[14]. The SA node is composed of specialized cells that exhibit automaticity and generate their own APs[14]. This impulse spreads across the atria through Bachman's Bundle, to the atrioventricular node, where conduction is delayed, allowing for proper ventricular filling, and then travels through the His-Purkinje network to allow for synchronized ventricular contraction[15]. On the electrocardiogram, these events correspond to a P wave representing atrial contraction, the QRS complex representing ventricular contraction, and the T wave representing ventricular repolarization. Disruptions in normal conduction or cardiomyocyte excitability can disturb the heart's coordinated rhythm (sinus rhythm) and promote arrhythmogenic conditions[16], which will be discussed in further detail in the sections below.

At the cardiomyocyte level, excitation-contraction coupling converts electrical impulses to mechanical contraction[17]. Depolarization of the cardiomyocytes triggers sodium influx, followed by the opening of L-type calcium channels on the T-tubules, allowing for an influx of Ca^{2+} into the cytosol[14]. The Ca^{2+} then binds onto ryanodine receptors on the sarcoplasmic reticulum (SR), allowing the release of a large amount of Ca^{2+} into the cytosol, in a process called calcium-induced calcium release[17]. This allows calcium to bind to troponin C on the actin filament, causing a conformational shift in tropomyosin that exposes myosin-binding sites on actin, enabling cross-bridge cycling and sarcomere shortening[17]. Relaxation occurs when calcium is taken back into the SR, while potassium efflux restores resting potential and enables repolarization[18].

Beyond excitation-contraction coupling within the individual cardiomyocytes, synchronized propagation of the AP through the myocardium determines the stability of the sinus rhythm. Conduction velocity (CnV) refers to the speed at which an electrical impulse travels through the myocardium[19]. This is dependent on the rate of individual cardiomyocyte depolarization and how effectively electrical current passes between them via gap junctions[19]. The refractory period (RP) defines the interval after depolarization during which cardiomyocytes cannot be re-excited, ensuring unidirectional impulse propogation[20]. Together, conduction velocity and refractory period determine cardiac wavelength, defined as the distance an impulse travels before the myocardium regains excitability[19,20]. A shorter cardiac wavelength, caused by slowed conduction or reduced RP, increases the likelihood of an arrhythmia occurring[19,20].

Atria and ventricles differ both structurally and functionally, with variations in wall thickness, chamber size, contractility, pressure generation, and underlying ion channel and electrophysiological characteristics[11,21]. The walls of the atria are structurally thinner and more compliant and are therefore subject to higher wall stress[22]. When compared to ventricular cardiomyocytes, atrial cardiomyocytes exhibit shorter RPs and APDs due to enhanced repolarizing potassium currents and reduced plateau calcium currents[23,24]. These structural and electrophysiological differences allow for rapid atrial conduction; however, this increases susceptibility to pathological remodelling[13,25]. Understanding these chamber-specific characteristics provides a foundation for interpreting how systemic and local stressors drive atrial remodelling and dysfunction in HFpEF, as explored in the following section.

1.3 Heart Failure: Definition, Classification, and Epidemiology

1.3.1 What is Heart Failure

HF has emerged as a major global health challenge, with U.S. prevalence projected to surpass eight million cases by 2030, corresponding to roughly one in 33 adults and an estimated economic burden of $70 billion annually[26]. HF is a clinical syndrome characterized by the heart's inability to deliver adequate blood flow to meet the body's metabolic requirements[27]. It arises from structural or functional abnormalities that elevate filling pressures and/or impair cardiac output at rest or during exertion[27]. Risk factors include hypertension, diabetes, and atherosclerotic cardiovascular disease[28]. Common causes of HF include ischemic heart disease, myocardial infarction, hypertension, and valvular heart disease[28]. Other causes include genetic or familial cardiomyopathies, infiltrative diseases such as amyloidosis, cardiotoxicity from cancer therapies or substance use (alcohol, cocaine, methamphetamine), tachycardia- or pacing-induced cardiomyopathies and stress-related cardiomyopathies, peripartum cardiomyopathy, myocarditis, autoimmune or inflammatory disorders, iron overload, and endocrine or metabolic abnormalities[28]. General symptoms include breathlessness, ankle swelling, fatigue, and exercise intolerance, which may be accompanied by elevated jugular venous pressure, pulmonary crackles, and peripheral edema[27,29].

HF is broadly classified into two major phenotypes: heart failure with preserved ejection fraction (HFpEF) and heart failure with reduced ejection fraction (HFrEF)[2]. EF is defined as the percentage of blood ejected from the left ventricle during each contraction[27]. HFpEF is classified as heart failure with an EF greater than or equal to 50%, whereas HFrEF is classified as having an EF less than or equal to 40%[3]. HFrEF is driven by contractile impairment, whereas HFpEF is characterized by preserved systolic function but impaired ventricular relaxation and increased myocardial stiffness[27,28]. These mechanistic differences underlie distinct clinical presentations and therapeutic responses. Unlike HFrEF, no therapy has consistently demonstrated efficacy in major clinical trials for HFpEF, largely due to the significant pathophysiological heterogeneity that characterizes this diverse condition[30].

1.3.2 Epidemiology and Defining Features of HFpEF

HFpEF now accounts for more than half of HF cases and is increasing relative to HFrEF, particularly due to the aging population and the increased prevalence of conditions predisposing to its development, including hypertension, obesity, metabolic syndrome, and diabetes[2,26]. It is most prevalent among older adults, particularly in women[31]. This condition is marked by substantial morbidity and mortality, with a 35% two-year rate of heart-failure hospitalization and a 14% two-year mortality rate[2]. The affected population is highly heterogeneous, exhibiting substantial variation in comorbidity profiles, disease severity, cardiac morphology, circulating biomarker patterns, and clinical outcomes, making this condition exceptionally difficult to diagnose and treat[26,30].

HFpEF patients present with impaired ventricular relaxation, increased myocardial stiffness, and elevated left ventricular filling pressures despite preserved EF[2]. These abnormalities contribute to pulmonary congestion, exercise intolerance, and reduced cardiac reserve[2,32]. In addition to concentric LV hypertrophy, atrial remodelling, and diastolic dysfunction, HFpEF also involves multiorgan pathology, including systemic and pulmonary vascular dysfunction, skeletal muscle impairments, and altered body composition[2].

HFpEF elicited by metabolic alterations, termed cardiometabolic HFpEF, is emerging as the most prevalent form, and when compared with non-cardiometabolic HFpEF, is characterized by more severe symptom burden and reduced quality of life[2,26]. Increasing evidence suggests that HFpEF is a systemic disorder driven by coexisting comorbidities, which contribute to disease development rather than serving as associated conditions[26]. Among these pathophysiological mechanisms, chronic low-grade inflammation has become a central driver, connecting metabolic dysfunction, vascular impairment, and myocardial remodelling[26,33]. Taken together, these factors drive the molecular and cellular processes examined in the next section. Figure 1 illustrates the downstream consequences of these comorbidities and how they collectively contribute to the development of HFpEF.

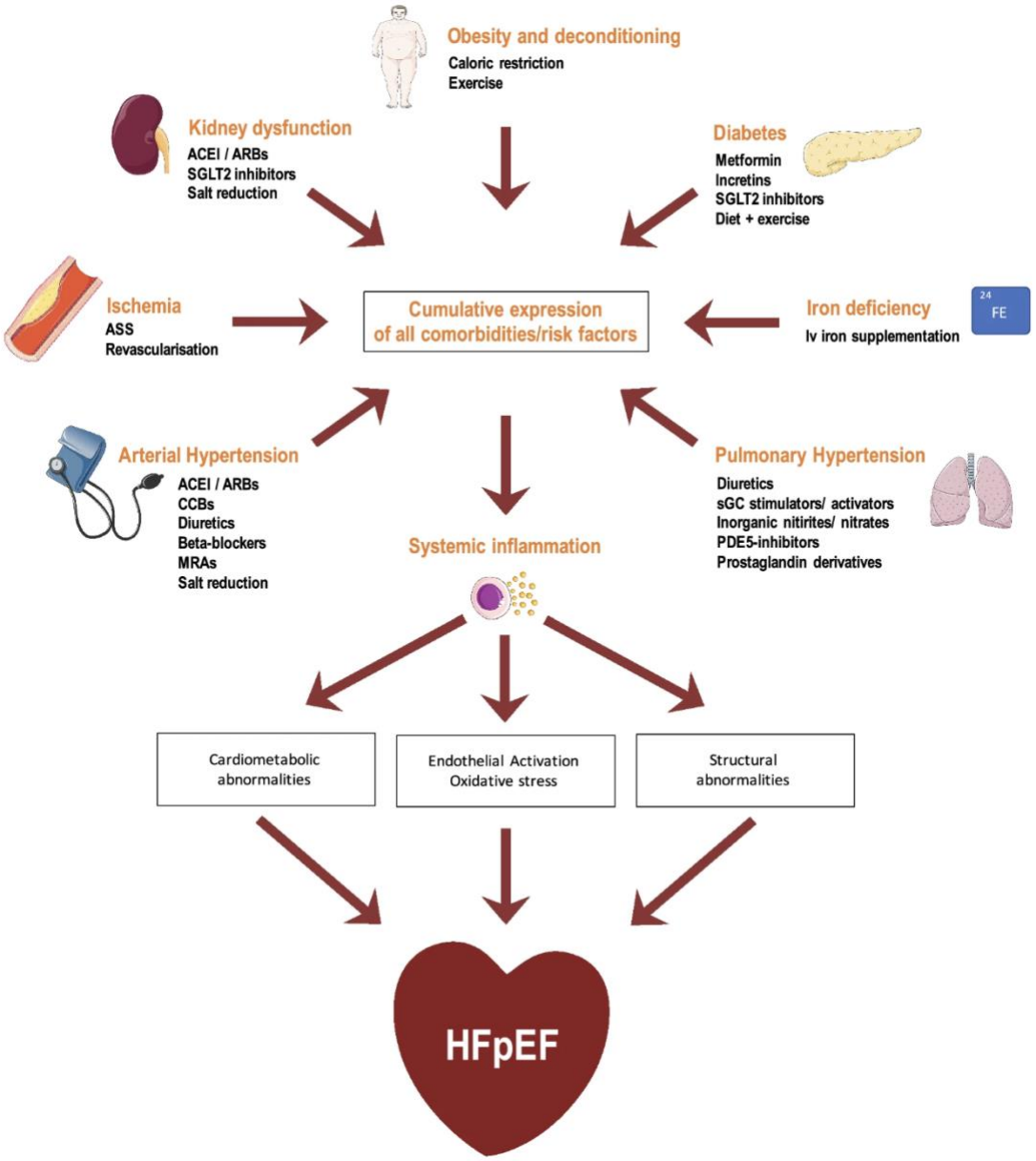

Figure 1. Effect of common cardiovascular comorbidities on systemic inflammation and HFpEF development. Multiple co-morbid conditions, including obesity, diabetes, iron deficiency, pulmonary hypertension, arterial hypertension, ischemia, and kidney dysfunction, act together to promote chronic systemic inflammation. This inflammatory state contributes to cardiometabolic abnormalities, endothelial activation with oxidative stress, and structural cardiac remodelling, which collectively reduce ventricular compliance and impair diastolic function. These processes ultimately lead to the development of HFpEF. Reproduced from Wintrich *et al.* Clinical Research in Cardiology (2020)[34], under the Creative Commons CC BY 4.0 license (https://creativecommons.org/licenses/by/4.0/). No changes were made.

1.4 Mechanistic Drivers of Cardiometabolic HFpEF

Cardiometabolic HFpEF represents a distinct and increasingly predominant endotype of HFpEF in which metabolic, vascular, and inflammatory stressors act together to promote cardiac remodelling and diastolic dysfunction[26]. When compared to non-cardiometabolic HFpEF, this subtype is characterized by more severe haemodynamic abnormalities, greater RV and LV maladaptive remodelling, reduced functional capacity and exercise tolerance, exacerbated diastolic dysfunction, and a biomarker profile consistent with increased inflammatory markers[26]. At the mechanistic level, cardiometabolic stressors such as obesity, hypertension, insulin resistance, and systemic inflammation initiate molecular and structural changes within the myocardium.

1.4.1 Cardiac Hypertrophy and Impaired Relaxation

Cardiomyocyte hypertrophy and stiffness are key determinants underlying diastolic dysfunction in cardiometabolic HFpEF[26]. Alterations in sarcomeric protein composition and post-translational modifications, specifically in titin, troponin I, myosin-binding protein C, and tropomyosin, play a key role in cardiomyocyte distensibility and compliance[26,35,36]. Hypophosphorylation of the N2B and PEVK segments of titin reduces myocardial elasticity, promoting diastolic dysfunction[26]. These modifications occur due to diminished protein kinase G (PKG) activity, resulting from disrupted endothelial NO–cGMP signaling associated with cardiometabolic comorbidities[26,33]. Comorbidities associated with HFpEF, especially obesity, induce a systemic proinflammatory state, resulting in coronary microvascular endothelial cells producing high levels of reactive oxygen species (ROS), which in turn limits bioavailability of nitric oxide (NO) for adjacent cardiomyocytes[33]. Limited NO bioavailability decreases PKG activity in cardiomyocytes, resulting in the hypophosphorylation of the cytoskeletal protein titin, thereby promoting cardiomyocyte hypertrophy [33].

The molecular defects that impair cardiomyocyte compliance also activate downstream signaling and transcriptional programs that drive hypertrophic growth and structural remodeling. The principal mediators behind cardiomyocyte hypertrophy include neurohormonal activation, notably by angiotensin II, catecholamines, and endothelin-1, and mechanical stress[26]. Together,

these initiate downstream signalling cascades that contribute to many pathogenic changes, including reactive oxygen species generation, inflammation, metabolic alterations, and fibrosis[26]. Epigenetic modifications, including histone modification, DNA methylation, and non-coding RNAs, have also been found to contribute to the regulation of hypertrophic growth and other pathogenic processes in cardiometabolic HFpEF[37.]

1.4.2 Inflammation in Cardiometabolic HFpEF

Cardiometabolic HFpEF is characterized by chronic low-grade inflammation, both systemically and at the cardiomyocyte level[33,38]. Prevalent comorbidities, including aging, hypertension, obesity, and diabetes, all contribute to the inflammatory state observed in this syndrome and their combined presence is believed to drive inflammatory processes in HFpEF, underlying a key pathophysiological mechanism[26,33]. Results of the PROMIS-HFpEF study suggest that inflammation is the link between comorbidity burden and structural remodelling, driving worsening diastolic stiffness and myocardial fibrosis[39]. Chronic low-grade inflammation has been found to increase cardiomyocyte hypertrophy and stiffness, extracellular matrix remodeling, oxidative/nitrosative stress, and mitochondrial and metabolic dysfunction[26]. It has also been proposed that systemic inflammation, driven by comorbidities, induces coronary microvascular endothelial inflammation, which in turn results in myocardial remodeling through endothelial oxidative stress, reduced NO bioavailability, and impaired downstream cGMP–PKG signaling[33].

At the molecular level, chronic inflammatory and oxidative stimuli from comorbidities, including TNFα, IL-6, and ROS, activate NF-κB–dependent transcription in endothelial and myocardial cells, driving the upregulation of iNOS[33,40,41]. This leads to S-nitrosylation of endoplasmic reticulum proteins and impaired protein handling, which contributes to cardiomyocyte dysfunction[42]. These effects are compounded by nitrosative and oxidative stress, which disrupt eNOS (endothelial nitric oxide synthase) signaling and further reduces NO–cGMP–PKG activity, central to microvascular endothelial inflammation and diastolic stiffening in HFpEF[26,33].

Obesity-induced adipose tissue expansion promotes macrophage infiltration and release of proinflammatory cytokines, resulting in metabolic inflammation (“meta-inflammation”), which contributes to the systemic low-grade inflammatory state present in HFpEF[26,33]. Epicardial

adipose tissue (EAT) plays an important role in the context of HFpEF due to its proximity to the myocardium[43]. EAT expansion is associated with worse hemodynamic parameters, impaired exercise capacity, increased HF hospitalizations, and higher all-cause mortality[26,44,45]. Increased EAT has also been associated with myocardial remodelling, such as increased fibrosis, as well as contributes to systemic inflammation, endothelial dysfunction, and insulin resistance[45,46]. EAT secretes inflammatory cytokines and adipokines that contribute to local and systemic inflammation, while also acting as a reservoir for various immune cell populations[26]. EAT induces cardiomyocyte hypertrophy and promotes myocardial insulin resistance through its metabolic activity[26].

1.4.3 Extracellular Matrix Remodelling

Cardiac fibrosis is characterized by the excessive accumulation of extracellular matrix (ECM) proteins, predominantly collagen I and III, within the myocardium following cardiac stress[47–49]. Although fibrogenesis preserves structural integrity under stress, excessive deposition and cross-linking increase myocardial stiffness and impair ventricular relaxation, resulting in diastolic dysfunction[50,51]. The extracellular matrix of the heart is composed of collagens, glycoproteins, proteoglycans, and elastins, all which work together to provide mechanical support and signaling roles through the myocardium[52,53]. Dysregulation of collagen turnover shifts the balance toward accumulation and cross-linking, elevating filling pressures and compromising diastolic performance[54]. Cardiac fibrosis can manifest in several forms, including reparative, reactive, or infiltrative[55]. Reparative fibrosis replaces necrotic myocardium after injury[55]. Infiltrative fibrosis results from the deposition of non-native materials such as amyloid[55]. Reactive fibrosis results in diffuse interstitial and perivascular collagen deposition in response to chronic stress or inflammation[49,55]. Reactive fibrosis in the LV is a pathological hallmark of adverse cardiac remodeling that contributes to both the development and progression of HFpEF[49].

ECM remodelling and increased myocardial interstitial fibrosis are central drivers of diastolic dysfunction in cardiometabolic HFpEF[26,33]. Histological analysis of HFpEF myocardium indicates increased collagen I expression, enhanced collagen cross-linking, and elevated collagen volume fraction, all which contribute to diastolic dysfunction[56]. In the context

of cardiometabolic HFpEF, the deposition of collagen in the myocardium occurs partly through the transformation of fibroblasts to myofibroblasts[33]. This process is stimulated by TGF-β released from infiltrating monocytes at sites of microvascular inflammation[33]. This inflammatory microenvironment also suppresses NO bioavailability, leaving the profibrotic effects of endothelin-1, angiotensin II, and aldosterone unopposed, thereby strengthening fibrotic signaling.[33] Inflammatory crosstalk with immune cells and adipose-tissue-secreted factors such as osteopontin further promotes profibrotic fibroblast transformation and myocardial dysfunction[26].

1.4.4 Metabolic Dysfunction

Cardiometabolic HFpEF is driven by significant mitochondrial and metabolic disturbances that impair cardiomyocyte energetics[26]. Decreased phosphocreatine to ATP ratios reflect diminished energy reserves and impaired ATP generation in patients with HFpEF[57]. Under metabolic stress, the heart exhibits reduced capacity to switch between energy substrates, reflecting metabolic inflexibility[26]. This is expressed by suppressed glucose oxidation alongside excessive but inefficient fatty acid oxidation, which results in lipid overload and elevated oxidative stress[26]. Metabolomic profiling shows downregulation of fatty-acid and glucose-metabolism genes, accumulation of branched-chain amino acids from impaired catabolism, and reduced β-hydroxybutyrate levels, all of which indicate disrupted energy substrate flexibility[58].

1.4.5 Insulin Resistance

Insulin resistance, a defining feature of obesity and diabetes, is highly prevalent in cardiometabolic HFpEF and drives widespread metabolic and inflammatory disturbances affecting both systemic and myocardial function[59]. Impaired insulin signaling through the IRS1/2–PI3K–Akt cascade reduces GLUT4-mediated glucose uptake and disrupts key downstream pathways regulating cardiomyocyte growth, autophagy, metabolism, and survival[26]. Insulin resistance is associated with increased circulating levels of triglycerides, fatty acids, and glucose, along with elevated concentrations of inflammatory cytokines, catecholamines, and growth hormones[26]. These systemic alterations are coupled with mitochondrial dysfunction,

oxidative stress, and endoplasmic reticulum stress, all which play a role in the pathogenesis of cardiometabolic HFpEF[26].

AMPK regulates contraction-induced GLUT4 translocation in cardiomyocytes and is a key regulator of multiple essential cellular processes[26]. Impaired AMPK activation contributes to the pathogenesis of insulin resistance, metabolic syndrome, and cardiometabolic HFpEF[26]. Pharmacologic activation of AMPK has been shown to restore insulin sensitivity and improve atrial remodelling in models of cardiometabolic HFpEF[26].

Insulin plays an important role in regulating lipid metabolism by suppressing lipolysis in adipose tissue. Under normal conditions, insulin inhibits the breakdown of triglycerides into free fatty acids (FFAs) and glycerol by suppressing the activity of hormone-sensitive lipase [60]. This limits circulating FFAs and promotes triglyceride storage via lipoprotein lipase activation and de novo lipogenesis[60]. In insulin-resistant states, inhibitory control is impaired, allowing excessive FFA release despite hyperinsulinemia[61]. The resulting elevation in circulating FFAs promotes ectopic lipid deposition, oxidative stress, and mitochondrial dysfunction in organs including the heart[61]. In cardiometabolic HFpEF, this dysregulated lipolytic activity contributes to myocardial lipid accumulation and energetic inefficiency, driving diastolic dysfunction and inflammatory remodelling[62,63].

1.4.6 Contributions of HFD, Sucrose, and L-NAME to HFpEF Pathophysiology

HFD, high-sucrose intake, and NOS inhibition by L-NAME are widely used in combination to model the cardiometabolic, hypertensive, and inflammatory features of HFpEF in rodents[2,42,64,65]. Chronic exposure to HFD induces obesity, dyslipidemia, and insulin resistance at the systemic level[66,67]. In visceral obesity, adipose tissue is infiltrated by macrophages, leading to the release of proinflammatory cytokines such as TNFα and IL-6[33]. These cytokines activate c-Jun N-terminal kinase (JNK) and IκB kinase β (IKKβ), which phosphorylate insulin receptor substrate-1 (IRS-1) on serine residues, thereby disrupting downstream activation of the PI3K–Akt signaling pathway[68–70]. Reduced Akt activity prevents GLUT4 translocation to the plasma membrane, impairing glucose uptake in skeletal muscle and cardiomyocytes[71,72]. Consequently, cardiomyocytes shift from glucose utilization toward fatty acid β-oxidation, which increases mitochondrial oxygen consumption but decreases ATP yield per oxygen molecule consumed[73].

This metabolic shift increases oxidative stress, activating redox-sensitive transcription factors such as NF-κB that perpetuate inflammatory signaling[74]. Excess fatty acid influx also leads to accumulation of toxic lipid intermediates, further impairing insulin signaling and inducing endoplasmic reticulum and mitochondrial stress[75]. These processes contribute to lipotoxicity, ROS generation, and progressive structural remodelling, culminating in LV concentric hypertrophy and diastolic dysfunction[62,76].

Chronic consumption of a high-sucrose diet induces metabolic, vascular, and myocardial abnormalities that collectively promote the HFpEF phenotype[77]. A high sucrose intake results in repeated postprandial spikes in glucose and insulin, stimulating lipogenesis by the liver, and increasing plasma triglycerides and non-esterified fatty acids[78]. This leads to increased transport of fatty acids and triglycerides to peripheral organs, notably the myocardium, along with high glucose availability[79]. This constant oversupply of glucose and lipid substrates overwhelms oxidative capacity, resulting in the generation of mitochondrial ROS and consequently lipid peroxidation[80]. This results in oxidative damage to cardiomyocytes and impairment of calcium-handling proteins such as SERCA2a, which delays relaxation and contributes to diastolic dysfunction[80,81].

High-sucrose diets also have a direct influence on endothelial and vascular function. Chronic hyperglycemia activates the polyol and hexosamine pathways, depleting NADPH and the increasing the generation of ROS[82]. This promotes eNOS uncoupling, leading to a reduction in NO bioavailability, which in turn increases vascular tone and stiffness, resulting in diminished coronary microvascular reserve[83]. Simultaneously, hyperglycemia promotes the formation of advanced glycation end-products (AGEs) in the plasma and tissues[84]. AGEs cross-link collagen and elastin, which stiffens the myocardial interstitium and reduces ventricular compliance, which promotes diastolic dysfunction[85]. Activation of RAGE by AGEs on endothelial and immune cells promotes downstream NF-κB signaling and NADPH oxidase activity, further increasing vascular oxidative stress and inflammation[86].

L-NAME is a non-selective inhibitor of NOS that blocks the enzymatic conversion of L-arginine to NO and L-citrulline[87]. It primarily inhibits eNOS and neuronal (nNOS) isoforms while having much lower potency toward inducible NOS (iNOS), and therefore mainly suppresses constitutive NO production involved in basal vascular tone and cardiomyocyte signaling rather than inflammation-induced iNOS activity[26,88]. Under normal physiological

conditions, NO diffuses to vascular smooth muscle cells and cardiomyocytes, activates soluble guanylyl cyclase (sGC), elevates cGMP, and stimulates PKG, which lowers intracellular Ca^{2+} and maintains vascular and myocardial relaxation[89].

Chronic L-NAME administration disrupts the NO–sGC–cGMP–PKG signaling pathway, resulting in persistent vasoconstriction, endothelial dysfunction, and arterial hypertension[90]. Arterial hypertension results in increased afterload, which in turn stimulates concentric left-ventricular hypertrophy as an adaptive response to pressure overload[91]. Reduced PKG activity within the myocardium results in hypophosphorylation of the N2B titin isoform, increasing passive stiffness and impairing diastolic relaxation[92]. Simultaneously, reduced NO bioavailability contributes to cardiac fibrosis by impairing cGMP signaling, which normally suppresses fibroblast activation[93]. Loss of the NO–cGMP pathway allows phosphodiesterase-2 activity to lower intracellular cAMP levels, promoting fibroblast-to-myofibroblast differentiation and extracellular matrix deposition[93]. Hypertension stresses the coronary microvasculature, activating endothelial cells to recruit monocytes, which become TGF-β–producing macrophages that stimulate fibroblasts to deposit collagen, ultimately leading to myocardial fibrosis[94].

Collectively, chronic exposure to a HFD, high-sucrose intake, and L-NAME work together to reproduce the complex cardiometabolic, vascular, and hemodynamic abnormalities characteristic of HFpEF. HFD primarily drives obesity, insulin resistance, and systemic inflammation, creating a metabolic environment that promotes myocardial lipid accumulation, oxidative stress, and concentric remodeling. The addition of a high-sucrose diet intensifies these effects by inducing recurrent hyperglycemia and endothelial dysfunction, increasing oxidative stress, and accelerating the formation of AGEs that stiffen the myocardium and vasculature. Chronic L-NAME administration leads to hypertension, impaired NO–cGMP–PKG signaling, titin hypophosphorylation, and cardiac fibrosis, further compromising diastolic relaxation and compliance. Together, these metabolic, vascular, and hypertensive stressors work simultaneously to drive the multifactorial pathophysiology of HFpEF observed in patients.

1.5 Left Ventricular Remodelling and Diastolic Dysfunction

Chronic cardiometabolic, vascular, and hypertensive stress collectively promote maladaptive LV remodelling and impaired diastolic function, both central characteristics of

HFpEF[33]. LV remodelling refers to structural and cellular adaptations of the myocardium to sustained mechanical, metabolic, or inflammatory stress[95]. Ventricular remodelling typically manifests as either concentric hypertrophy, where wall thickness increases while chamber volume remains stable, or eccentric hypertrophy, characterized by ventricular dilation and thinning of the myocardial wall[96]. HFpEF is associated mainly with concentric remodelling driven by prolonged pressure overload, in contrast to the eccentric remodeling observed in HFrEF, which develops under conditions of volume overload[96]. While concentric hypertrophy initially compensates by normalizing wall stress, persistent metabolic and hemodynamic strain ultimately promotes myocardial stiffening and diastolic dysfunction[97].

1.5.1 Hemodynamic and Stretch-Mediated Remodelling

Pressure overload refers to the chronic increase in systolic wall stress that occurs when the heart must pump against an elevated afterload, such as when a person is hypertensive[98]. To compensate, the LV thickens to normalize stress and maintain CO[98]. This hypertrophic response is mediated by mechanosensitive signaling pathways including angiotensin II, endothelin-1, MAPK, and calcineurin–NFAT, which drive protein synthesis and re-expression of fetal genes such as β-MHC, ANP, and BNP, a classic feature of pathological hypertrophy[99]. Sustained myocardial stretch also promotes the release of profibrotic factors such as TGF- β and connective tissue growth factor[100]. These factors activate fibroblasts and enhance collagen synthesis, which results in reduced compliance and increased passive tension in the LV[100]. Over time, this adaptive remodelling becomes pathological, characterized by thicker walls with reduced diastolic compliance and higher passive stiffness[97].

1.5.2 Metabolic, Inflammatory, and Age-related Mechanisms

As mentioned in the previous sections, metabolic stress from high-fat and high-sucrose intake enhances oxidative stress and suppresses NO–cGMP–PKG signaling, which is a key mechanism underlying diastolic dysfunction in HFpEF[33]. Reduced PKG activity leads to hypophosphorylation of the N2B titin isoform, increasing cardiomyocyte passive tension[26]. Inflammatory cytokines such as TNFα and IL-6 contribute to endothelial inflammation and paracrine signaling that promote fibroblast activation, extracellular matrix deposition, and

increased myocardial stiffness[33]. Aging further contributes to diastolic dysfunction through endothelial NO deficiency, mitochondrial ROS accumulation, and impaired ATP generation[101]. The aging myocardium also exhibits greater collagen cross-linking via increased AGEs, increasing passive stiffness, and reduced SERCA2a activity, which delays calcium reuptake and prolongs relaxation[102,103]. These factors predispose older hearts to HFpEF, even without major comorbidities.

1.5.3 Functional Implications of LV Remodeling

The diastolic, or filling phase, of the cardiac cycle can be divided into two components[32]. First, the left ventricle transitions from a contracted to a fully relaxed state, referred to as active relaxation, which is an energy-dependent process requiring ATP for calcium reuptake into the sarcoplasmic reticulum[32]. The subsequent passive filling phase reflects the ventricle's elastic properties and compliance, as the myocardium stretches in response to blood inflow without additional energy consumption[32]. A hemodynamic study by Zile et al. (2004) demonstrated that patients with HFpEF exhibit abnormalities in both phases, characterized by impaired active relaxation and increased passive stiffness[104].

The combined effects of pressure overload, metabolic stress, inflammation, and aging lead to elevated left ventricular end-diastolic pressure, delayed relaxation, and increased myocardial stiffness, which collectively result in pulmonary congestion and exercise intolerance, defining features of the HFpEF phenotype[101]. Persistent elevation of LV filling pressures transmits to the left atrium, causing stretch-mediated dilation, fibrosis, and electrical remodeling, which links ventricular diastolic dysfunction to the characteristic atrial pathology observed in HFpEF[95,101]. The effects of metabolic co-morbidities and hypertension on the development of diastolic dysfunction, which characterises HFpEF, is summarized in Figure 2.

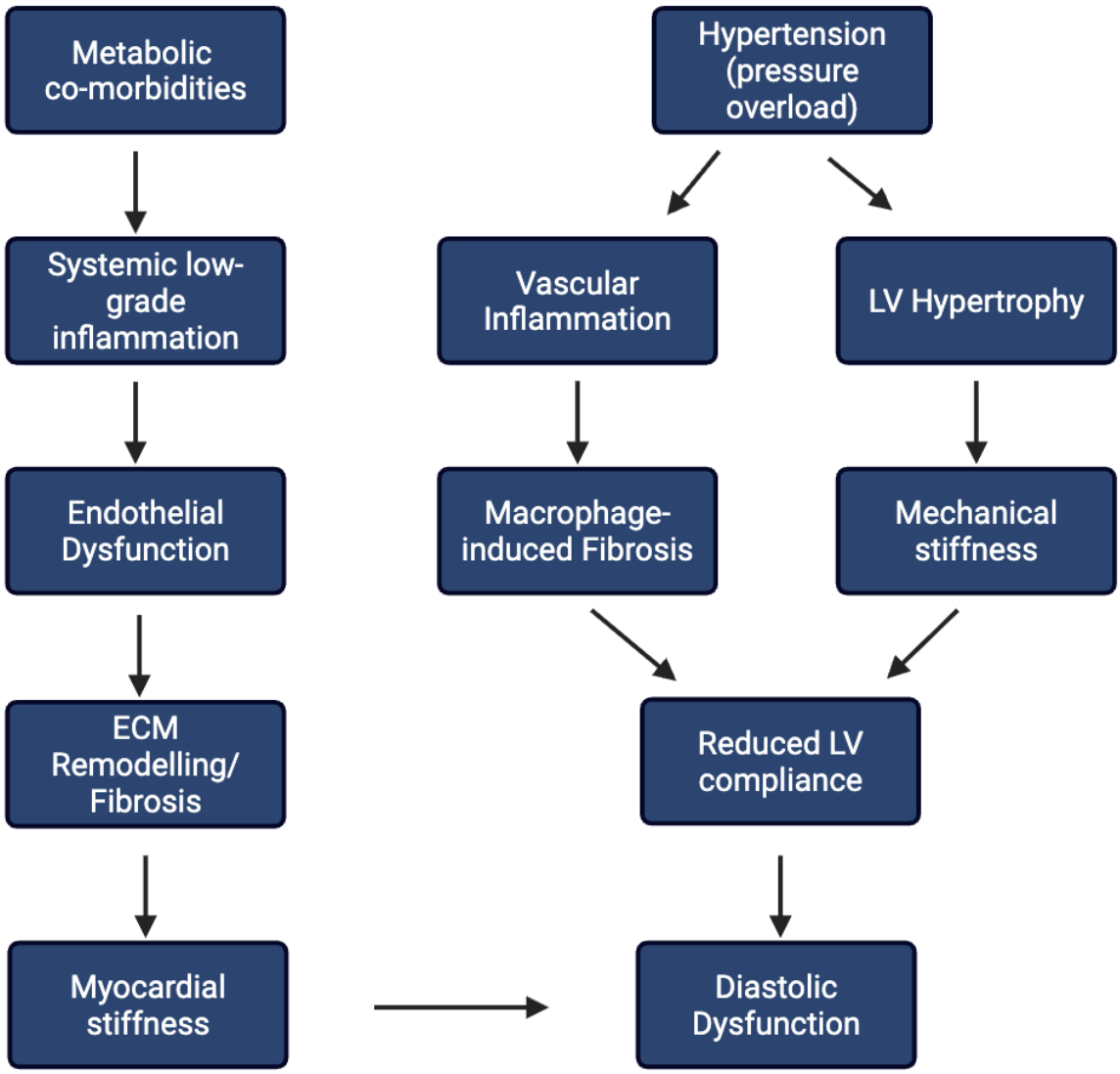

Figure 2. Effect of metabolic co-morbidities and hypertension on development of diastolic dysfunction. Metabolic comorbidities, such as obesity and type II diabetes, induce systemic low-grade inflammation, resulting in endothelial dysfunction, including the coronary microvasculature, which then drives extracellular-matrix remodelling and reactive fibrosis in the myocardium, driving myocardial stiffness and diastolic dysfunction. Pressure overload, due to arterial hypertension, results in both vascular inflammation and hypertrophic remodelling of the left ventricle Vascular inflammation results macrophage-induced fibrosis, while hypertrophy drives mechanical stiffness, both which reduce LV compliance and result in diastolic dysfunction, which characterises HFpEF. Figure was created in Biorender.com.

1.6 Atrial Remodelling in HFpEF

Chronic elevation of LV pressures due to diastolic dysfunction elevates LA filling pressures, where increased mechanical load introduces structural, cellular, and inflammatory changes that progressively impair atrial compliance, contractile function, and electrophysiology, referred to as atrial remodelling[105,106]. This haemodynamic stress on the LA initially drives compensatory dilation to maintain atrial function, but over time, sustained stretch and extracellular matrix activation become maladaptive and elicit progressive atrial myopathy, driving the development of AF[106,107]. Collectively, these mechanisms explain why HFpEF is so frequently accompanied by AF, which can both precede and follow the development of HFpEF. Figure 3 illustrates this bidirectional relationship.

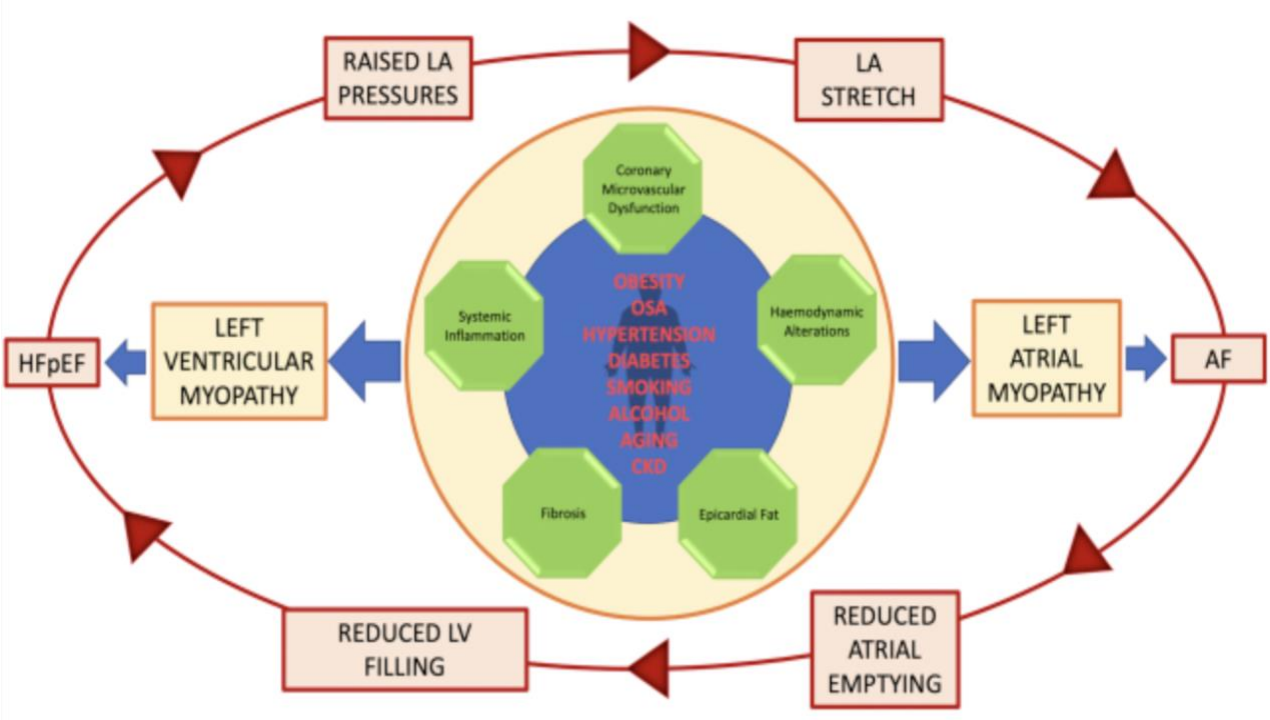

Figure 3. Mechanisms underlying coexisting AF and HFpEF. Cardiovascular comorbidities, including obesity, hypertension, and diabetes, promote systemic inflammation, fibrosis, and endothelial dysfunction, and haemodynamic alterations. These processes drive structural and functional remodelling in both the atria and ventricles, leading to LA and LV myopathies that predispose to AF and HFpEF. Once established, AF and HFpEF exacerbate one another through impaired left-atrial function, creating a positive feedback that accelerates disease progression. Reproduced from Ariyaratnam *et al.*, Heart Rhythm O2, 2021[108], under the Creative Commons CC BY-NC-ND license (http://creativecommons.org/licenses/by-nc-nd/4.0/). No changes were made.

1.6.1 Structural Remodelling

Persistent mechanical stress activates profibrotic signaling cascades, including TGF-β, platelet-derived growth factor, renin–angiotensin–aldosterone system, and endothelin-1, that stimulate fibroblast activation and collagen I/III deposition, resulting in interstitial and perivascular fibrosis[106]. Recent studies have shown that fibrosis initiates in regions of high wall stress, particularly adjacent to the pulmonary vein ostia and posterior wall and progresses to diffuse interstitial and perivascular fibrosis with disease advancement[106]. Simultaneously, EAT surrounding the atria expands and secretes pro-inflammatory cytokines such as TNFα, IL-6, and monocyte-chemoattractant protein-1 (MCP-1), promoting oxidative stress and myofibroblast differentiation[109]. Together, these factors drive LA concentric remodelling with increased wall thickness and reduced distensibility[110].

1.6.2 Functional Remodelling

During early disease progression, impaired LV active relaxation reduces suction during early diastole, shifting greater responsibility to the LA[111]. To compensate, atrial contractility and booster-pump function must increase to maintain stroke volume[107]. However, as mechanical load and fibrosis increase, the left atrium undergoes functional remodelling characterized by a progressive decline in its reservoir, conduit, and booster-pump functions[106]. During ventricular systole, atrial reservoir function declines because fibrotic stiffening and reduced wall elasticity limit LA expansion, thereby impairing its ability to store pulmonary venous return[106,112]. This loss of compliance also elevates mean LA pressure, reducing the pressure gradient between the pulmonary veins and LA and promoting pulmonary congestion[111]. In early diastole, impaired LV active relaxation reduces suction, which then diminishes the transmitral pressure gradient, causing a reduction in the LA's conduit function[106]. Instead of blood flowing passively from the LA to the LV, a larger fraction remains in the atrium, further increasing atrial pressure and wall stress[111]. As disease progression worsens, the sustained afterload and cardiomyocyte hypertrophy impair the LA's contractility, and the booster-pump function deteriorates as atrial contractile reserve is exhausted[106]. This results in reduced late-diastolic LV filling, increased pulmonary pressures, and exercise intolerance[112].

1.6.3 Inflammatory Mechanisms in Atrial Remodelling

In cardiometabolic HFpEF, systemic metabolic comorbidities, including obesity, diabetes, and hypertension, create chronic low-grade inflammation that extends into the atrial myocardium[33]. Macrophages have been found to play a key role in the inflammatory remodelling that takes place[33,113]. Resident F4/80$^+$ cardiac macrophages normally support tissue homeostasis and matrix turnover, whereas infiltrating CCR2$^+$ monocyte-derived macrophages adopt a more pro-inflammatory, pro-fibrotic state[114]. In HFpEF-associated inflammation, macrophages shift toward a proinflammatory phenotype, characterized by increased secretion of TNF-α, IL-1β, and IL-6, along with diminished reparative signaling[115]. This increases oxidative stress and recruits additional monocytes through CCR2-dependent chemotaxis, which strengthens local inflammation and promotes extracellular matrix remodelling through fibroblast activation and collagen synthesis[116]. Cytokines released by activated macrophages, together with ROS-induced oxidative stress, stimulate endothelial cells to secrete additional inflammatory mediators and undergo endothelial-to-mesenchymal transition, producing fibroblast-like cells that contribute to collagen deposition and expansion of the profibrotic cell population[33,117].

Simultaneously, EAT, which lies in direct contact with the atrial myocardium, is expanded and inflamed in HFpEF, highlighting the metabolic and inflammatory burden associated with obesity, diabetes, and hypertension[118]. Under these conditions, EAT acts as a paracrine organ that releases inflammatory and profibrotic mediators that diffuse into the atrial myocardium and recruit CCR2$^+$ monocytes, promoting macrophage activation and polarization toward a proinflammatory phenotype that further amplifies cytokine release and fibroblast activation[119]. EAT also produces ROS and adipokines that activate TGF-β/SMAD2-3 signaling in atrial fibroblasts, which induces collagen I/III expression and myofibroblast differentiation[120]. Overall, these interactions cause fibrotic remodelling and atrial stiffening, establishing the mechanical and electrical disturbances that define atrial remodelling in HFpEF[121].

Together, the structural, functional, and inflammatory remodelling that occurs creates an atrial environment highly susceptible to electrical instability, establishing the arrhythmogenic substrate that facilitates atrial fibrillation development in HFpEF.

1.7 Atrial Remodelling in AF

Our grasp of AF pathophysiology has dramatically improved in the past years, mainly due to improved recognition of the importance of atrial remodelling, which refers to any persistent change in atrial structure or function[25]. Atrial stretch, caused by elevated pressure associated with volume overload, resulting from hypertension, heart failure, and mitral valve disease, is a main contributor to atrial remodelling[122]. Atrial stretch has been observed to trigger a mechanical inflammatory response, which further induces remodelling, including fibrosis[122]. To maintain structural integrity in the atria following stretch-induced inflammation, fibrosis develops, and CnV is slowed as a result of the consequent conduction block[8,123]. Atrial fibrosis stimulates heterogeneous atrial depolarization, providing the structural remodelling necessary for electrical re-entry and subsequent AF[124].

In the case of HFpEF and metabolic disorders associated with AF, adipocyte infiltration has been recognized as an additional factor in the remodelling of the atria by influencing CnV[125]. With an increase in EAT, adiposity, cytokines, free fatty acids, and other bioactive molecules accumulating within the myocytes, normal impulse initiation and propagation properties of the myocardium are altered[126]. Adipocyte infiltration into the myocardium can lead to non-uniform propagation of an activation wave front[127]. The adipose tissue separates cardiomyocytes, creating a barrier that forces the electrical impulse to divert from its path, slowing conduction velocity[127]

1.8 Electrophysiological Mechanisms of Atrial Fibrillation

1.8.1 Re-entry and Electrophysiological Determinants

AF is maintained by propagating re-entrant wavelets, which require a susceptible substrate and trigger (provided by ectopic firing)[25,128]. To maintain re-entry, the conduction time, determined by circuit path length and CnV, must be greater than the longest refractory period (RP) in the circuit[25]. Long path lengths and slowed CnV increase circuit time, allowing enough time for all points in the circuit to be re-excited by the re-entering impulse[25]. RP determines the recovery of excitability in conductive tissue; therefore, a shortened RP increases the probability that tissue can be re-excited when a re-entrant impulse conducts through the tissue[25].

Cardiac wavelength depends on the relationship between CnV and RP[128]. It describes the path length the depolarization wave covers throughout the functional refractory period[128]. Wavelength is obtained by the product of CnV and the effective refractory period (ERP)[128]. A decrease in either ERP duration or CnV will decrease wavelength, and a greater number of wave fronts can circulate through the atria, and AF may be sustained[128,129]. The number of wavelets that can occupy the surface of the atria at any one time is influenced by the size of the atria, CnV, and ERP[128]. Re-entry is therefore favoured by a longer distance of the impulse circuit resulting from atrial enlargement, shortening of the ERP promoted by an increase in outward potassium currents or decrease in inward calcium currents, and slowed CnV induced by cellular and tissue structure changes, including fibrosis, connexin expression/localization, and adipocyte infiltration[25]. Methods to increase conduction velocity and/or refractoriness may protect against AF initiation, maintenance, and recurrence[130].

1.8.2 Gap Junction Remodelling and Ionic Regulation of Refractoriness

Altered gap junction expression and localization is another factor that influences CnV in the atria[8]. The electric conduction of the myocardium is provided by gap junctions, cell-to-cell connections that preserve low-resistance intercellular coupling through specialized hemichannel subunit proteins termed connexins (Cx)[131]. Cx43 and Cx40 are the principal gap junctional subunits in the atria[131]. Abnormal electrical coupling between cardiomyocytes, resulting from structural alterations in connexin distribution and protein levels, has been associated with enhanced susceptibility to AF and is common in patients and experimental animals with AF[131,132]. Gap junction remodelling is characterized by altered channel expression, subcellular distribution from the intercalated discs to the lateral membrane, conductance, and permeability (determined by phosphorylation of the Cxs)[132]. Variations in any of these factors will negatively impact myocardial synchronization in the heart and contribute to AF inducibility[132].

As mentioned, a reduced atrial ERP (eARP) will result in a shorter wavelength, allowing for a greater number of wavefronts to circulate through the atria, sustaining AF. The length of the action potential duration (APD) directly influences the duration of the eARP[25,129]. When APD is decreased, the eARP duration is shortened. This can result from an intrinsic change in ion channel expression in the cardiomyocytes themselves or from extrinsic innervation from the

autonomic nervous system[133–136]. Intrinsic changes that result in reduced eARP are accomplished primarily by ICaL downregulation and via increased inward-rectifier K currents[25,129]. Shortening of eARP can also result from a change in autonomic tone, as either vagal or sympathetic activation can shorten eARP[129]. eARP is also regulated by vagal activity via the acetylcholine-dependent inward-rectifier current (IKACh)[8]. Increased activity of IKACh abbreviates atrial APD, and therefore eARP[137]. Recent studies have looked at the role of calcium-activated potassium channels in AF pathophysiology and therapy[138]. The small-conductance KCa 2 (SK2) channel was found to play a central role in cardiac repolarization and has recently been the target of therapeutics for atrial tachycardias[139].

1.9 TNFα-Mediated Mechanisms in Heart Failure

TNFα is a cytokine with pleiotropic biological capacities, including proinflammatory capabilities. It has been identified as a key factor in the pathology of exercise-induced AF, with TNFα gene ablation observed to prevent AF vulnerability and structural remodelling of the atria in response to exercise[8]. Clinical data have indicated that proinflammatory molecules play a key role in the development and progression of HF and have also detected myocardial infiltration by inflammatory cells[2]. Since the early 1990s, researchers have observed elevated levels of TNFα in patients with HF, suggesting a role of inflammation in the pathology of HF[140,141]. In 2004, a soluble TNFα antagonist, etanercept, was used in clinical trials as a possible therapeutic to alleviate the HFrEF phenotype, however found no benefit and had adverse effects including increased risk of hospitalizations and death[142,143].

1.9.1 Myogenic Response

Recent studies have suggested that the failed clinical trials occurred because acute inhibition of the TNFα-induced myogenic response drastically reduces total peripheral resistance (TPR), and therefore mean arterial pressure (MAP), which can result in death in HFrEF patients[143]. The myogenic response is an intrinsic property of small resistance vessels that enables them to constrict or dilate in response to changes in intraluminal pressure, thereby stabilizing blood flow to tissues[143]. When arterial pressure rises, the vessel wall stretches,

triggering smooth-muscle contraction that narrows the lumen and limits blood flow, whereas when pressure falls, the muscle relaxes and the vessel dilates[143]. This mechanism is essential for maintaining TPR and, consequently, MAP under normal physiological conditions[143].

In HF, as CO declines, the maintenance of MAP increasingly depends on vascular tone[143]. Recent studies have found that TNFα plays a key role in myogenic responsiveness in HF[143]. The TNFα/Sphingosine-1-Phosphate signaling axis is responsible for driving this myogenic responsiveness, acting as the key mechanism that converts changes in transmural pressure into vasoconstrictive tone[143]. Through this pathway, TNF-α maintains the basal myogenic activity required to preserve TPR when CO falls[143,144].

In early stages of HF, this TNFα-dependent vasoconstriction is beneficial, as it sustains MAP and perfusion pressure despite impaired cardiac function[143]. However, as the disease progresses, the response becomes maladaptive, as persistent myogenic vasoconstriction elevates afterload, further reducing CO and impairing tissue perfusion[143]. Eventually, TPR reaches its maximal limit while CO continues to decline, resulting in a drop in MAP, which is now primarily governed by the failing heart rather than vascular compensation[143].

Because TNF-α is required for myogenic vasoconstriction, its inhibition effectively eliminates the myogenic response, resulting in a severe reduction in TPR and MAP[144]. This loss of vascular tone explains the adverse hypotensive outcomes observed in anti-TNF clinical trials for HFrEF, where perfusion pressure was already low. Experimental deletion or pharmacologic blockade of TNF-α eliminates pressure-induced constriction and produces systemic hypotension across species, including humans[144]. In contrast, because hypertension is the most common comorbidity associated with HFpEF, the reduction in TPR resulting from TNF-α inhibition may not have the same detrimental effects and could even be beneficial by alleviating excessive vascular tone[143,144].

1.9.2 TNFα-dependent activation of iNOS

Studies have observed that TNFα can modulate cardiovascular performance via activation of inducible nitric oxide synthase (iNOS)[145]. When TNFα binds its receptor, an intracellular signalling pathway is initiated, leading to the translocation of nuclear factor kappa B (NF-κB) into the nucleus and subsequent transcription and expression of iNOS[40,41]. A recent

study has provided evidence that the activation of iNOS is a key mechanism in triggering nitrosative stress in HFpEF and observed that when iNOS is either genetically silenced or pharmacologically inhibited, the HFpEF phenotype is ameliorated[2,42].

Because TNFα acts upstream of this signalling pathway, it is likely an important regulator of NF-κB-mediated iNOS activation and the resulting nitrosative stress. Consistent with this, the same study reported a significant increase in TNFα mRNA expression (fold change) in a HFpEF model utilizing HFD and L-NAME, suggesting that elevated TNF-α may drive iNOS induction and contribute to the development of oxidative and nitrosative injury observed in this condition[42].

1.10 Rationale and Knowledge Gap

HFpEF now accounts for more than half of all HF cases, with its prevalence only increasing[26]. It encompasses a highly diverse patient population characterized by substantial variation in comorbidity burden, disease severity, cardiac structure, circulating biomarkers, and clinical outcomes, underscoring its heterogeneity[26,33]. This complexity has made it increasingly more difficult to identify a unifying mechanism or to develop therapeutic targets[33]. Recent work has emphasized that HFpEF represents a complex, comorbidity-driven, multisystemic disorder in which accompanying conditions such as obesity, hypertension, diabetes, and systemic inflammation are not simply coincidental but play an active role in disease progression[26]. Increasing evidence has identified chronic low-grade inflammation as a key driver of HFpEF pathogenesis[26,33]. Among inflammatory cytokines, TNFα is consistently elevated in both patients and experimental models of heart failure and is associated with adverse cardiac and vascular remodelling[146].

AF is highly prevalent in HFpEF, with approximately two-thirds of patients either presenting with or eventually developing AF, reflecting the well-established clinical overlap between AF and HFpEF[2]. Substantial evidence now supports that AF is strongly influenced by inflammatory mechanisms rather than being solely an electrical disorder[147,148]. Among inflammatory mediators, TNFα has been repeatedly implicated[8]. Elevated TNFα levels correlate with AF burden, and experimental studies show that TNFα inhibition or gene deletion reduces atrial fibrosis, improves conduction properties, and lowers susceptibility to AF[8]. Because HFpEF

arises from chronic metabolic, hypertensive, and vascular stressors that elicit a robust systemic and myocardial inflammatory response, this provides a biologically relevant context to investigate how inflammation differentially affects the atria compared with the ventricles.

TNFα acts upstream of the NF-κB/iNOS axis[40,41]. Upregulated iNOS generates sustained NO production that reacts with superoxide to form peroxynitrite, driving nitrosative stress and myocardial dysfunction[42]. Genetic deletion or pharmacological inhibition of iNOS alleviates diastolic dysfunction and fibrosis in HFpEF mouse models, supporting a causal link between nitrosative stress and the phenotype[42]. Moreover, increased TNFα mRNA expression has been observed in HFpEF models induced by HFD and L-NAME, suggesting that TNF-α serves as an upstream inflammatory trigger linking cytokine signalling to iNOS activation[42].

Recent studies have demonstrated that the TNFα/sphingosine-1-phosphate signalling axis is required for myogenic responsiveness in resistance vessels, the intrinsic mechanism that stabilizes TPR and MAP[143,144]. Pharmacological TNFα inhibition using etanercept abolishes this response and markedly lowers MAP in multiple species, confirming the dependence of systemic haemodynamics on TNFα myogenic tone[143,144]. Clinical trials targeting TNFα in HFrEF, notably the ATTACH (infliximab) and RENEWAL (etanercept) studies, reported no therapeutic benefit and, in some cases, increased mortality[142,149]. Because hypertension is the most common comorbidity in HFpEF, reductions in TPR produced by TNF-α inhibition may not trigger hypotension to the same extent as in HFrEF and could even be beneficial in certain hypertensive phenotypes[143].

Although prior work has identified TNFα as an important inflammatory mediator in HFpEF, its role in shaping chamber-specific remodelling remains unresolved. In particular, it is unknown whether the inflammatory environment generated by HFpEF disproportionately affects the atria in a way that directly promotes an arrhythmogenic substrate, or whether TNFα serves as the upstream driver of these atrial-ventricular differences. This gap is significant because AF is highly prevalent in HFpEF, however, the mechanistic link between the HFpEF phenotype and increased atrial susceptibility has not been defined at the level of cytokine-dependent remodeling. Therefore, the key unanswered questions are whether HFpEF induction produces distinct atrial versus ventricular structural and functional changes, and whether TNFα is responsible for these divergent responses. Understanding these mechanisms provides the basis for the present study.

1.11 Hypotheses and Objectives

1.11.1 Hypotheses

1. HFpEF induction in mice will produce a differential remodeling response in the ventricles and atria, and the resulting atrial structural, functional, and inflammatory changes will establish a mechanistic link between the HFpEF phenotype and increased susceptibility to atrial fibrillation.
2. The inflammatory factor TNFα is required for the induced chamber specific differences observed in the HFpEF model

1.11.2 Objectives

The objectives of this study were as follows:

1. Characterize the chamber specific responses of a HFpEF model using a combination of high fat diet feeding, high sucrose supplementation, and L-NAME administration in a CD1 mice strain.

Additional objectives not achieved

2. Determine the effects of TNFα inhibition on the HFpEF phenotype using the developed HFpEF murine model.
3. Determine the fundamental mechanisms through which TNFα inhibition confers protection against the HFpEF/AF phenotype.

Chapter 2: Materials and Methods

2.1 Experimental Animals

Male CD1 mice bred in-house were randomly assigned to either the experimental group or the control group at 6–8 weeks of age. CD1 mice from Charles River were also used, however, had feces from the in-house mice mixed into bedding in order to normalize gut microbiome. The experimental group received a high-fat diet (D12492, Research Diets) with L-NAME (1–1.5 g/L, Thermo Scientific) administered in their drinking water after adjusting the pH to 7.4, with the addition of 12% (w/v) sucrose in the drinking water, prepared using commercially available granulated sugar (Rogers, Lantic Inc., Canada). The controls were maintained on a standard chow diet (LabDiet 5015) with access to regular tap water. Mice were maintained on their respective diets for a duration ranging from 12 to 18 weeks. All animals were housed under identical environmental conditions on a 12:12 hour light-dark cycle. Mice had ad libitum access to their assigned diets and water throughout the study. All experimental procedures were conducted in accordance with the guidelines established by the Canadian Council on Animal Care and were approved by the Animal Care Committee at York University.

2.2 Exercise Exhaustion Test

After three days of acclimatization to treadmill exercise, an exhaustion test was performed on the experimental groups of mice. The test was conducted on an inclined treadmill set at a 10° incline (Panlab, Harvard Apparatus). Mice first acclimated at a speed of 0 m/min for 5 minutes, followed by sequential increases to 5 m/min for 5 minutes, 10 m/min for 10 minutes, and then 15, 20, and 25 m/min for 5 minutes each, as described in Beyfuss *et al.* 2018. The exhaustive phase then began, during which the speed was increased by 1 m/min every 3 minutes until exhaustion[150]. Exhaustion was defined as the inability of a mouse to resume running within 5 seconds of contact with the electric stimulus grid. Total running time was recorded, and running distance was calculated accordingly.

2.3 Echocardiography

Echocardiographic evaluations of left ventricular function were conducted in mice under general anesthesia. Anesthesia was initiated by exposing the animals to a 3% isoflurane–oxygen mixture in an induction chamber. Once anesthetized, mice were positioned supine on a heated platform, and anesthesia was maintained via a nose cone delivering approximately 1.5% isoflurane in oxygen, as described previously[151]. Core body temperature was continuously tracked using a rectal temperature probe (THM 150; Indus Instruments, Webster, TX, USA) and kept within a physiological range of 36.9°C to 37.3°C. Respiratory rate was maintained between 90 and 120 breaths per minute through minor adjustments to the isoflurane concentration. Electrocardiographic monitoring was performed using the lead II configuration. To optimize ultrasound transmission, chest fur was removed with a depilatory cream (Nair; Church and Dwight, Princeton, NJ, USA), and acoustic gel (Aquasonic 100; Parker Laboratories Inc., Fairfield, NJ, USA) was applied to the thoracic surface. Structural and functional parameters of the left ventricle were obtained using a high-resolution 30 MHz linear ultrasound transducer (Vevo 2100; Visual Sonics Inc., Toronto, ON, Canada) in both B-mode and M-mode transthoracic imaging configurations.

2.4 Intraperitoneal Glucose Tolerance Test

Intraperitoneal glucose tolerance tests were conducted to evaluate systemic glucose handling in mice following a fasting period of 6 hours. After the fasting period, each mouse received an intraperitoneal injection of D-glucose (1.5 g/kg body weight) prepared in sterile saline (0.9% NaCl)[152]. Blood glucose levels were measured at baseline (0 minutes, before glucose administration) and subsequently at 15-, 30-, 45-, 60-, and 120 minutes post-injection using a handheld glucometer and test strips calibrated for mouse blood glucose (mg/dL)[152]. Blood samples were obtained via a small tail vein poke using a sterile needle. Throughout the procedure, mice were gently restrained to minimize stress, and care was taken to limit the total blood volume collected. All measurements were performed in a consistent environment to reduce variability due to temperature or handling.

2.5 Effective Refractory Period and Arrhythmogenic Inducibility Measurements

Mice were anesthetized using the same protocol described for echocardiographic measurements[151]. This protocol was described previously in Aschar-Sobbi *et al.* 2015. To access the right jugular vein, a superficial incision was made through the skin, followed by gentle blunt dissection to separate and retract the overlying muscle and connective tissue. Once exposed, a suture was placed around the anterior portion of the jugular vein to secure it. A small incision was then created posterior to the suture, allowing for the insertion of a 2-Fr octopolar recording and stimulation catheter (CI'BER Mouse; NuMed, Hopkinton, NY, USA). A second suture was tied around the catheter at the site of insertion to stabilize it within the vessel. The catheter was then advanced through the superior vena cava into the right atrium and subsequently into the right ventricle. Proper positioning was confirmed by identifying a distinct His bundle depolarization waveform on the electrogram, recorded between electrodes 3 and 4 of the octopolar catheter, along with the appropriate waveform in each respective channel.

A 15-minute stabilization period was allowed prior to the initiation of all electrophysiological recordings. Timed bipolar electrical stimulation was delivered to targeted cardiac regions (specifically the atria or ventricles) using adjacent electrode pairs on the octopolar catheter and a programmable stimulator with cycle control (Pulsar 6i; Frederick Haer Co., Bowdoin, ME, USA). Intracardiac electrograms were recorded from selected bipolar electrode configurations on the catheter, along with surface ECG signals acquired via subdermal needle electrodes positioned to capture lead II. All signals were amplified and digitized using a multichannel acquisition system (Gould ACQ-7700; Data Sciences International), and data was analyzed using P3 software (Data Sciences International).

To determine the stimulation threshold required for electrical capture, pacing pulses were applied between adjacent electrodes on the octopolar catheter at intervals 20 milliseconds below the intrinsic R–R interval. The voltage was gradually increased until consistent cardiac capture was observed, indicated by the appearance of QRS complexes following each stimulus. All stimulation protocols used to evaluate atrial refractoriness or to induce atrial fibrillation were conducted using stimulation voltages set at 1.5 times the previously established capture threshold.

Atrial effective refractory periods were measured using field stimulation via bipolar lead pairs 7–8 or 5–6 of the octopolar catheter. Each assessment consisted of a train of nine stimuli

(S1 pulses) delivered at a constant cycle length, followed by a single premature pulse (S2). The S2 stimulus was initially introduced at a coupling interval below the expected capture threshold (~15 ms) and incrementally increased in 5 ms steps until consistent atrial capture was observed, as indicated by QRS complexes on the ECG. Once capture was achieved, the S2 interval was gradually decreased in 1–2 ms steps until capture was lost. Two independent measurements were obtained for each mouse, and the average of these values was reported as the AERP.

To assess atrial arrhythmia susceptibility, rapid programmed electrical stimulation was applied to the high right atrium (lead 7–8), followed by identical protocols delivered to the mid-atrium (lead 5–6). Two stimulation protocols were used: (i) 27 pulses of 1 ms duration delivered at a 40 ms cycle length, progressively shortened by 2 ms intervals down to 20 ms, repeated three times; and (ii) 20 pulses of 1 ms duration delivered at a constant 20 ms cycle length, repeated 20 times with 1.5-second pauses between trains[8]. This second protocol was followed by a 5-minute rest period and repeated up to three times. Ventricular arrhythmia inducibility was assessed using the same stimulation sequences applied to lead 1–2. Sustained arrhythmias were defined as reproducible episodes of rapid, irregular, and continuous atrial or ventricular activity lasting longer than 10 seconds.

2.6 Invasive Haemodynamics

Hemodynamic assessments were performed in mice anesthetized as described previously in the echocardiographic measurements[151]. The following protocol was described previously in Gorman *et al.* 2024. Following anesthetization, a midline incision was made just below the chin to expose the right common carotid artery. The salivary glands were gently retracted, and the carotid artery, identified by its location parallel to the trachea, was carefully dissected from surrounding connective tissue, taking care to avoid damage to the adjacent vagus nerve. A suture was placed around the anterior portion of the artery, and two additional sutures were positioned posteriorly: one served as a temporary ligature to minimize blood loss, and the other was used to secure the catheter following insertion. A small ventral incision was then made in the artery to allow the insertion of a 1-Fr pressure-transducing catheter (Scisense, London, ON, Canada), which was advanced retrogradely through the proximal aorta into the left ventricle.

Hemodynamic signals were recorded at a sampling frequency of 5000 Hz using the Scisense ADV500 control unit (Scisense, London, ON, Canada) and acquired with AcqKnowledge software (Biopac Systems Inc., Goleta, CA, USA). Prior to data collection, a minimum of 15 minutes was allotted to allow for physiological stabilization, ensuring a core body temperature of 36.9–37.3 °C and a respiratory rate of approximately two breaths per second. Following stabilization, five minutes of baseline pressure data were recorded.

2.7 Heart Isolation

Prior to tissue collection, mice were administered an intraperitoneal injection of heparin (0.2 mL of 1000 IU/mL; Leo Pharma, Thornhill, ON, Canada) to prevent blood clot formation. Anesthesia was induced using a 3% isoflurane-oxygen mixture, and a toe-pinch reflex was performed to confirm the absence of responsiveness. A ventral midline incision was made from the abdomen to the chest, followed by two lateral incisions at the base of the sternum extending toward the dorsal side to expose the diaphragm, as described previously[153]. The diaphragm was incised to open the thoracic cavity and allow access to the heart. After removal of the pericardium and lungs, and severing of the aorta, the heart was excised. It was then rinsed in 0.01 M phosphate-buffered saline (PBS) to remove residual blood, blotted dry, and weighed. The right hindlimb was also collected and placed in a bleach solution to expose the tibia, the length of which was measured using calipers to normalize heart weight.

2.8 Cardiac Perfusion and Fixation

For histological and immunohistochemical analysis, the inferior vena cava was transected following thoracic cavity exposure. Cardiac arrest in diastole was induced by injecting approximately 5 mL of 1% potassium chloride (KCl) in 0.01 M PBS into the apex of the heart using a 25-gauge needle[153]. This was immediately followed by perfusion with 20 mL of 4% paraformaldehyde (PFA) in 0.01 M PBS to achieve tissue fixation. The heart was then extracted as described above. Following extraction of the heart, subsequent processing steps varied depending on the intended embedding approach. Hearts were either prepared for cryosectioning

in Optimal Cutting Temperature (OCT) or processed for paraffin embedding, as described in the following sections.

2.9 Lung Wet-to-Dry Weight Measurements

Lung fluid content was assessed using the wet-to-dry weight method[42]. During terminal tissue collection, immediately prior to cardiac perfusion and heart removal, both the left and right lungs were excised and gently blotted to remove surface moisture. Whole lungs were weighed immediately to obtain the wet weight. Samples were then placed in a 37°C drying oven for 48 hours to allow complete desiccation. After drying, lungs were reweighed to obtain the dry weight. Lung wet-to-dry ratios were calculated for each animal by dividing the wet weight by the corresponding dry weight, providing an index of pulmonary fluid accumulation.

2.10 Paraffin Histology and Immunohistochemistry

Following excision, hearts were immersed in 35 mL of 4% paraformaldehyde (PFA) in 0.01 M phosphate-buffered saline (PBS) and fixed overnight at 4°C. The next day, hearts were washed three times in PBS for one hour each to remove residual fixative. They were then cleaned of any excess connective or adipose tissue and bisected along the coronal plane with a scalpel to expose the four-chamber view. Samples were placed into labeled cassettes and processed through a graded ethanol dehydration series (70%, 80%, 95%, 100%, 100%), followed by clearing with xylene (a 1:1 mixture of 100% ethanol and xylene, then two changes of 100% xylene), as described previously[153]. Tissues were then incubated in paraffin at 60°C for three consecutive changes to ensure complete infiltration. The following morning, samples were embedded in paraffin blocks. Serial sections were cut at 5 μm thickness using a microtome, mounted onto Superfrost Plus–charged glass slides, and left to dry overnight at room temperature.

For histological analysis, paraffin-embedded sections were deparaffinized through a series of 5-minute xylene treatments (two washes in xylene followed by a xylene–ethanol mixture), followed by sequential 5-minute ethanol washes (100%, 100%, 95%, 70%, and 50%), and finally rinsed in tap water for 10 minutes. Cardiac collagen content in atrial and ventricular tissue was assessed using Picrosirius Red staining, with sections incubated in the stain for 1 hour

at room temperature while shaking[153]. Slides were then rinsed twice in 0.5% acetic acid, dehydrated through graded ethanol washes (95%, 95%, 100%, and 100%), cleared in xylene (x3), and mounted with coverslips using toluene-based mounting medium (Fisher Scientific, Waltham, MA, USA).

High-resolution images of the left atrium and ventricle were captured using the Brightfield EVOS AutoFlo 2 microscope, with full tissue sections scanned at 20× magnification. Collagen quantification was performed using ImageJ software, applying a thresholding method that detects collagen based on its increased brightness relative to surrounding myocardial tissue. Collagen area was expressed as a percentage of total tissue area using pixel-based measurements. The analysis excluded pericapsular fibrosis, focusing exclusively on interstitial collagen within the left atrial appendage and left ventricular free wall.

For immunohistochemical detection of cardiac macrophages, paraffin-embedded heart sections were stained using a rat anti-mouse F4/80 primary antibody (Bio-Rad), followed by a goat anti-rat Alexa Fluor 647 secondary antibody (Invitrogen). Slides were deparaffinized as previously described and then rinsed in running tap water for 10 minutes[153]. Antigen retrieval was carried out using heat-induced epitope retrieval by submerging slides in 10 mM sodium citrate buffer containing 0.05% Tween-20 (pH 6.0) and heating them in a boiling pressure cooker. Once full pressure was reached, retrieval was maintained for 3 minutes, followed by a 10-minute rinse in tap water. Slides were subsequently washed three times for 5 minutes each in a wash buffer consisting of Tris-buffered saline (TBS; 2.42 g Tris base, 8 g NaCl, 70 mL ddH_2O) with 250 µL of Triton X-100 (pH 7.6). A hydrophobic barrier pen was used to circle the three tissue sections on each slide. To block nonspecific binding, sections were incubated for 1.5 hours in a blocking buffer composed of 1% bovine serum albumin (BSA), 10% goat serum, and 0.3 M glycine in PBS-Tween-20. After blocking, sections were washed three times in wash buffer (5 minutes each) and incubated overnight at 4°C with the primary antibody diluted 1:100 in PBS-T containing 1% BSA. Two of the three tissue sections were incubated with the primary antibody solution, while the third received only the dilution buffer and served as a negative control. After a 12-hour incubation, slides were rinsed three times in wash buffer and incubated for 1 hour at room temperature with the secondary antibody (1:100 dilution), which also included wheat germ agglutinin (WGA) to label cell membranes. This was followed by three additional 5-minute washes in wash buffer. Cellular nuclei were then counterstained with DAPI to stain cell nuclei,

followed by two final 3-minute washes. Finally, slides were mounted using an aqueous mounting medium consisting of Tris buffer, N-propyl gallate, and glycerol (pH 8.5).

Three images were acquired from the left atrial appendage and the left ventricular free wall using the EVOS AutoFlo 2 microscope. Image analysis was performed in ImageJ using a combination of the rolling ball background subtraction algorithm, thresholding, and binary conversion to ensure accurate identification of stained cells. Macrophages were defined as cells that co-expressed both F4/80 and DAPI signals. Only signals with a minimum of five overlapping pixels were considered to be true colocalization events. Total macrophage counts were normalized to tissue area using the WGA channel as a reference for tissue boundaries.

2.11 Statistical analysis

Summary data are presented as Mean ± SEM unless otherwise stated. Statistical assessments included unpaired Student's t-tests for two-group comparisons, with Welch's correction applied when variances were unequal. Non-parametric data were analyzed using Mann–Whitney U tests. Longitudinal measurements, including body-weight trajectories and glucose tolerance curves, were evaluated using two-way repeated-measures ANOVA or mixed-effects models with appropriate post-hoc corrections. A significance threshold of $p \leq 0.05$ was applied for all analyses, which were performed using GraphPad Prism.

Chapter 3: Results of HFpEF Model Characterization

3.1 Development and Characterization of the HFpEF Model

The first objective of this study was to develop and characterize a murine HFpEF model using a combination of HFD feeding and L-NAME supplementation in the CD1 mouse strain, which has never been developed or characterized in this context. Our approach was based on the HFpEF model introduced by Schiattarella et al. (2019), whose work demonstrated that combining HFD (Appendix A.1) with L-NAME produces a robust metabolic–hypertensive phenotype[42]. This model was selected because it recapitulates key clinical features, including preserved systolic function with impaired diastolic relaxation, metabolic dysfunction, exercise intolerance, myocardial hypertrophy, hypertension, and pulmonary congestion.

To replicate and refine this model, we initially followed the protocol established by the Hill laboratory. In our pilot study, seventeen mice (n=17) received HFD supplemented with 0.5 g/L L-NAME, while three mice (n=3) were maintained on a normal diet and water as controls. The intervention was sustained for eight weeks, during which body weight gain and water/L-NAME consumption were monitored. At the experimental endpoint, mice underwent a comprehensive assessment including exercise tolerance testing, intraperitoneal glucose tolerance (IPGTT), transthoracic echocardiography, intracardiac electrophysiology, and invasive haemodynamic recordings. Hearts and lungs were collected for histological analysis and wet–dry ratio measurements, respectively.

Although this initial protocol produced some HFpEF-like features, the haemodynamic abnormalities were modest and variable, consistent with reports that the HFD + L-NAME model can vary considerably between laboratories. To intensify the phenotype, we incorporated high sucrose supplementation, as prior studies have shown that adding sucrose to a high-fat regimen exacerbates metabolic stress, hypertension, and cardiac dysfunction[64,65,154]. Through repeated adjustments of L-NAME concentration, sucrose content, and intervention duration, we refined the protocol to 1.0 g/L L-NAME with 12% sucrose in the drinking water. We did not include additional control groups, such as HFD alone, L-NAME alone, sucrose alone, or any of their pairwise combinations, because previous studies have already characterized the effects of each of these interventions individually. Our goal in this thesis was to first establish and characterize the

combined model. Future work will incorporate these control groups to determine the specific contribution of each component. Importantly, several cohorts were intentionally extended beyond the standard 12-week protocol, with some run to 15, 17, and 18 weeks. These extended cohorts were used to determine whether a longer duration of the HFD + L-NAME + sucrose intervention produced additional changes in glucose tolerance, exercise capacity, or echocardiographic parameters. Across these longer-duration cohorts, we observed no meaningful differences compared to the 12-week groups. Metabolic, functional, and structural parameters plateaued, and the HFpEF phenotype was already fully established by 12 weeks. Extending the intervention did not deepen the severity of the phenotype or provide additional insight.

Two early CD1 cohorts obtained from Charles River were excluded because they failed to gain weight and consistently fought. Although these animals were the same strain, we considered the possibility that vendor-specific microbiome differences contributed to their abnormal response. To limit this variability, all subsequent Charles River cohorts received bedding supplemented with fecal material from our in-house CD1 colony before starting the diet in order to normalize gut microbiota.

Across the extended-duration cohorts, a small number of mice developed severe complications late in the intervention and were removed according to humane endpoint criteria. These animals were excluded from all analyses. Considering that the HFpEF phenotype was consistently present by 12 weeks, that prolonging the diet did not enhance the model, and that continued exposure increased the likelihood of adverse outcomes, all later cohorts were restricted to 12 weeks. This resulted in final cohort sizes of n = 14 for the normal-diet group and n = 21 for the HFDLS group.

Because the model-optimization phase included cohorts run for different durations, all animals were pooled together for analysis, and all physiological, metabolic, haemodynamic, structural, and inflammatory data in this thesis represent endpoint measurements collected at each cohort's terminal time point. No data are stratified by week or by duration category. The only exception is the body-weight trajectory, which is plotted across the full 18-week period to illustrate the stability and progression of weight gain over time. All other findings are presented as unified endpoint data from the final refined HFpEF model.

3.1.1 Physiological Characterization of the HFpEF Model

To determine whether the combined HFD + L-NAME + sucrose (HFDLS) intervention induced a physiological phenotype consistent with HFpEF, we evaluated a range of metabolic, functional, and cardiovascular parameters across cohorts. These assessments included longitudinal body weight tracking, glucose tolerance testing, exercise tolerance, transthoracic echocardiography, intracardiac electrophysiology, invasive haemodynamic measurements, and lung wet:dry ratios to assess pulmonary congestion. Together, these complementary measurements enabled comprehensive characterization of systemic metabolic responses, cardiac function, haemodynamics, electrophysiology, and pulmonary involvement associated with HFpEF. The following sections summarize the physiological features observed across these domains.

3.2 Metabolic Assessments

3.2.1 Diet-Induced Alterations in Body Weight

Percentage body-weight gain was monitored weekly to assess longitudinal metabolic responses to the HFD + L-NAME + sucrose (HFDLS) intervention. Mixed-effects modeling (REML) revealed significant main effects of Time ($p < 0.0001$) and Diet ($p < 0.0001$), as well as a significant Time × Diet interaction ($p < 0.0001$), indicating that % body-weight gain trajectories diverged between groups over the course of the intervention. Sidak-corrected pairwise comparisons showed that HFDLS mice exhibited significantly greater % body-weight gain than ND controls beginning at Week 3 ($p = 0.0485$), with progressively larger differences from Weeks 4–18 ($p = 0.0006$ to < 0.0001). These findings demonstrate that the HFDLS intervention produced a robust and sustained increase in % body weight gain relative to normal diet feeding (Figure 4A).

To compare overall weight gain between the two groups, percent body weight change from baseline to the final recorded week was calculated for each animal (varying from 12-18 weeks). HFDLS mice exhibited markedly greater weight gain (70.81 ± 3.44%) compared with ND controls (45.95 ± 2.23%). Because group variances were unequal ($p = 0.02$), the comparison

was evaluated using an unpaired two-tailed t-test with Welch's correction, which showed significantly greater percent weight gain in HFDLS mice ($p < 0.0001$) (Figure 4B). Together, these results indicate that chronic high-fat, high-sucrose feeding enhances weight gain and establishes a strong metabolic phenotype in this HFpEF model.

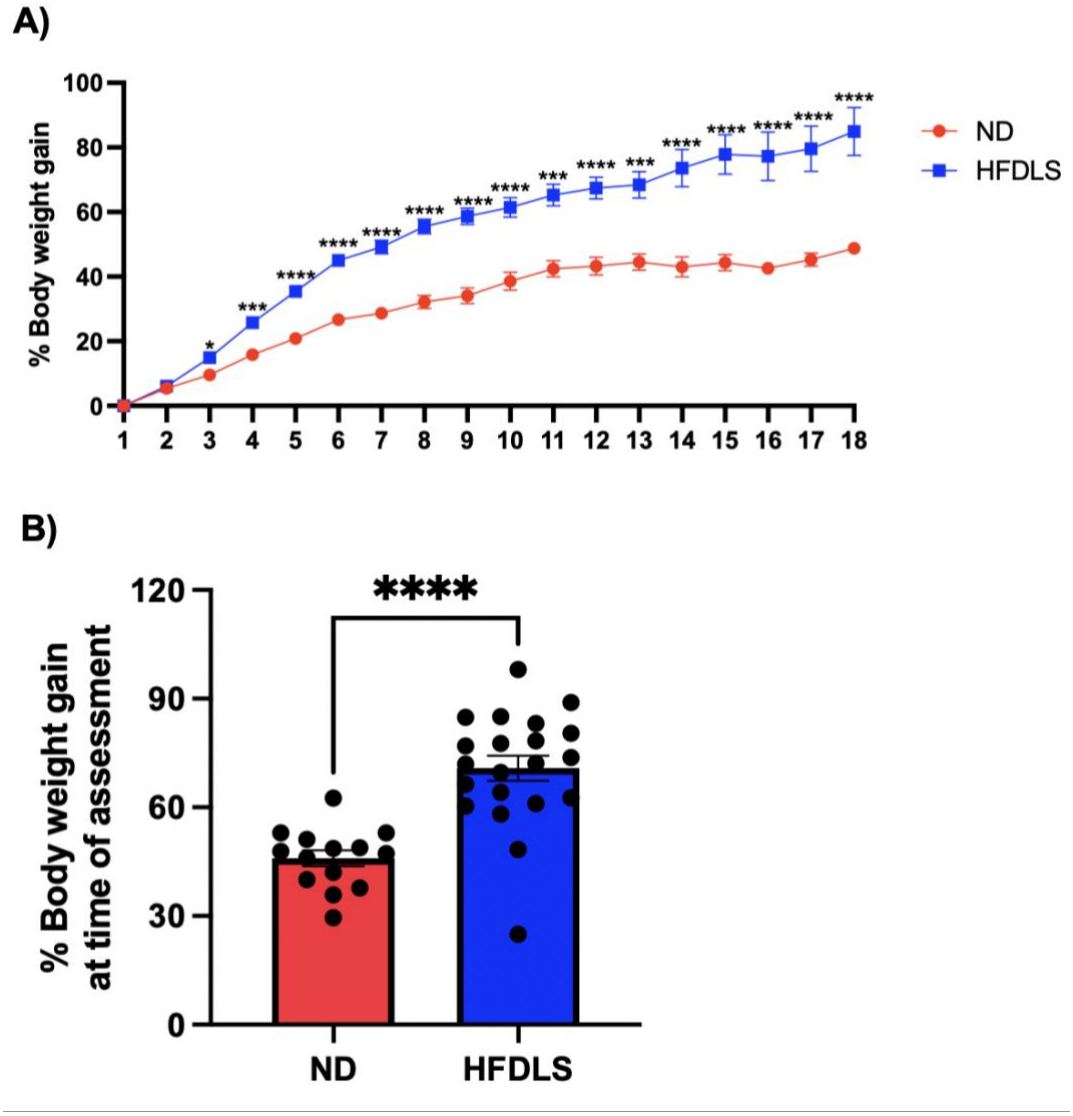

Figure 4. Effects of HFD + L-NAME + sucrose on percentage body-weight gain. Longitudinal metabolic responses were assessed in normal diet (ND; n = 14) and high-fat, L-NAME, sucrose (HFDLS; n = 21) mice. A) Percentage body-weight gain was monitored weekly across the feeding period. B) Percent body-weight gain from baseline to endpoint, varying from 12-18 weeks of the diet intervention. Data are presented as mean ± SEM. Statistical comparisons were performed using mixed-effects modeling (REML) with Sidak's multiple comparisons test (A) and an unpaired two-tailed t-test with Welch's correction (B). Significance levels: $p < 0.05$ (*), $p < 0.01$ (**), $p < 0.001$ (***), $p < 0.0001$ (****).

3.2.2 Glucose Tolerance

To further assess whether these differences in body weight were accompanied by alterations in systemic glucose handling, an intraperitoneal glucose tolerance test was performed (Figure 5A). Both ND (n = 6) and HFDLS (n = 12) mice exhibited a rapid rise in blood glucose concentrations within the first 30–45 minutes after glucose administration, followed by a gradual decline toward baseline by 120 minutes. Although HFDLS mice consistently displayed higher glucose values at each time point relative to ND controls, two-way repeated-measures ANOVA demonstrated a significant main effect of time ($p < 0.0001$) but no significant diet × time interaction (ns, $p = 0.118$) and no significant main effect of diet (ns, $p = 0.146$). These results indicate that while glucose levels changed over time as expected following glucose challenge, HFDLS mice did not show statistically significant impairments in glucose tolerance at individual time points compared with ND mice.

To quantify overall glycemic exposure, area under the curve (AUC) was calculated for each mouse (Figure 5B). HFDLS mice exhibited a higher mean AUC compared with ND controls (32,097 ± 3,055 vs. 25,188 ± 2,533), reflecting a modest upward trend toward increased overall glycemic exposure in response to glucose challenge. However, this difference was not statistically significant (ns, $p = 0.162$) when assessed using an unpaired two-tailed t-test. Together, these findings indicate that although HFDLS mice demonstrated numerically greater glucose exposure, neither the change in glucose over time nor the total glucose response differed significantly from ND mice.

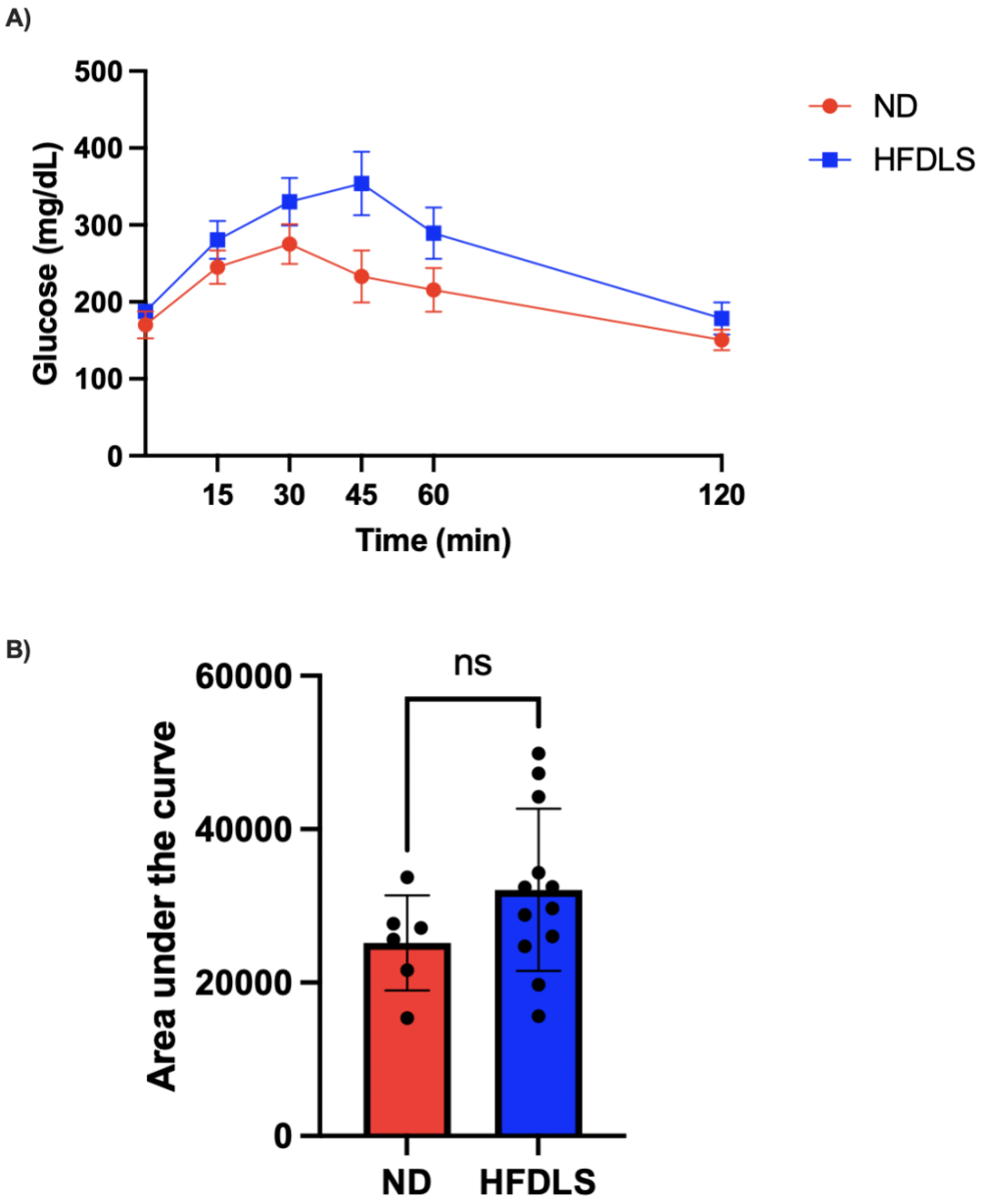

Figure 5. Impaired glucose handling in HFDLS mice demonstrated by intraperitoneal glucose tolerance testing. A) Blood glucose concentrations during the intraperitoneal glucose tolerance test (IP-GTT) in ND (n = 6) and HFDLS (n = 12) mice following 12–18 weeks of dietary intervention. Both groups exhibited a rapid rise in glucose within the first 30–45 minutes after glucose administration followed by a gradual decline toward baseline. Although HFDLS mice displayed numerically higher glucose levels across multiple time points, two-way repeated-measures ANOVA showed a significant main effect of time ($p < 0.0001$), but no significant main effect of diet (ns, $p = 0.146$) or diet × time interaction (ns, $p = 0.118$).B) Area under the curve (AUC) analysis of glucose excursions during the IP-GTT. HFDLS mice demonstrated a greater mean AUC compared with ND mice (32,097 ± 3,055 vs. 25,188 ± 2,533), indicating a modest upward trend toward increased cumulative glycemic response; however, this difference did not reach statistical significance (unpaired two-tailed t-test, ns, $p = 0.162$).

3.2.3 Exercise Tolerance

Following the assessment of metabolic status, exercise tolerance was evaluated to determine whether the HFDLS intervention impaired physical performance. HFDLS mice demonstrated a marked reduction in voluntary running performance compared with ND controls (Figure 6). An unpaired two-tailed t-test with Welch's correction revealed a significant decrease in total running distance in HFDLS mice ($p = 0.0008$). ND mice ran substantially farther than HFDLS mice (408 ± 31 m, $n = 14$ vs. 276 ± 9 m, $n = 21$), reflecting a clear deficit in exercise tolerance associated with the HFDLS intervention, consistent with early HFpEF-like functional limitation.

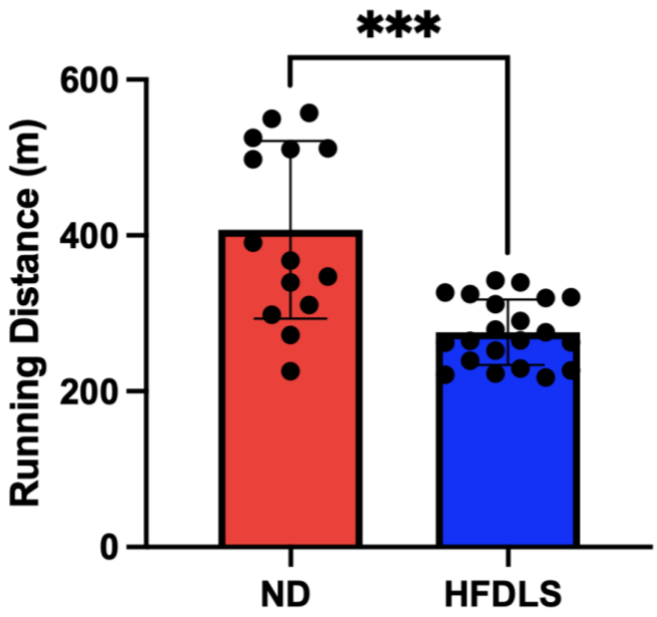

Figure 6. HFDLS Mice Display Reduced Exercise Capacity. An incremental treadmill exhaustion test was used to assess exercise tolerance in ND ($n = 14$) and HFDLS ($n = 21$) mice. Running distance to exhaustion was quantified and plotted with individual data points (Figure 3). Data are presented as mean ± SEM. An unpaired two-tailed t-test with Welch's correction revealed significantly reduced running distance in HFDLS mice compared with ND ($p = 0.0008$). Significance level: $p < 0.001$ (***).

3.3 Morphometric Assessment

Because HFpEF is defined not only by metabolic and functional impairment but also by concentric cardiac remodeling and elevated pulmonary pressures, we next quantified heart weight and lung wet-to-dry ratios to assess hypertrophic and congestive changes in this model.

3.3.1 Heart Weight

To assess cardiac hypertrophy, heart weight was normalized to tibia length (HW:TL) in ND and HFDLS mice (Figure 7). Mean HW:TL values were slightly higher in HFDLS mice, with ND mice exhibiting 13.11 ± 0.70 mg/mm, n = 14 and HFDLS mice exhibiting 14.78 ± 0.94 mg/mm, n = 21. Because the HFDLS group did not meet normality criteria, group comparisons were performed using a Mann–Whitney U test. This analysis showed no significant difference (ns, $p = 0.6298$) in HW:TL between groups. Although three HFDLS mice exhibited higher HW:TL values than the rest of the group, these measurements were considered biologically plausible and were therefore retained in the analysis.

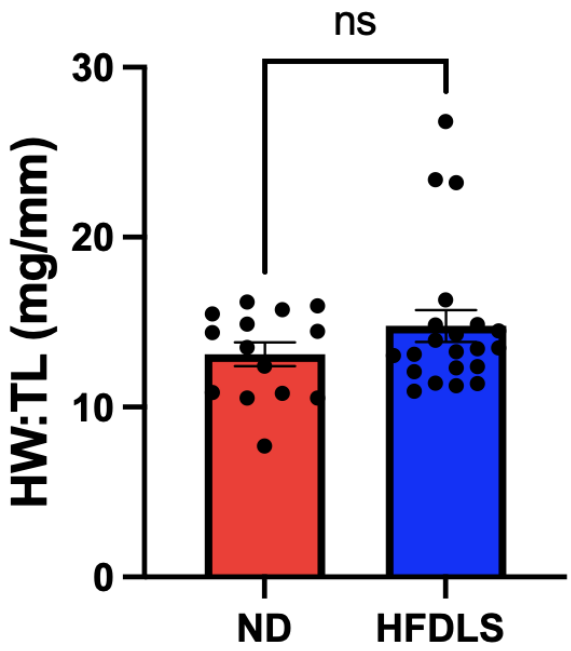

Figure 7. Heart weight normalized to tibia length does not differ between ND and HFDLS mice. HW:TL was measured at endpoint to assess cardiac hypertrophy, with tibia length used for size normalization. HFDLS (n = 21) mice showed a modest upward trend relative to ND (n = 14), but values were not significantly different. ND mice had a mean HW:TL of 13.11 ± 0.70 mg/mm and HFDLS mice had a mean HW:TL of 14.78 ± 0.94 mg/mm. Because the HFDLS group did not meet normality (Shapiro–Wilk $p < 0.0001$), groups were compared using a Mann–Whitney U test, which showed no significant difference (ns, $p = 0.6298$).

3.3.2 Lung Weight

To evaluate pulmonary congestion and fluid accumulation, which is a hallmark of HFpEF, lung wet-to-dry ratios were compared between ND and HFDLS mice (Figure 8). ND mice had a mean lung wet:dry ratio of 4.31 ± 0.10, n = 12, while HFDLS mice had a mean ratio of 4.33 ± 0.06, n = 18. An unpaired two-tailed t-test showed no significant difference (ns, $p = 0.877$) between groups. Overall, these data indicate that the HFDLS intervention did not induce detectable pulmonary edema at the time of collection.

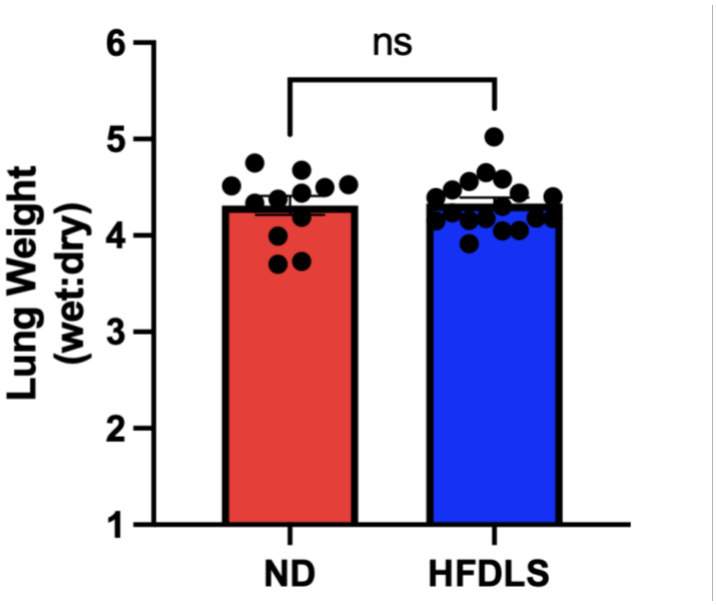

Figure 8. HFDLS feeding does not alter lung wet-to-dry ratios. Lungs were collected during terminal tissue extraction, weighed immediately after excision, dried for 48 hours at 37°C, and reweighed to obtain wet and dry weights. Lung wet:dry ratios did not differ between dietary groups. ND mice had a mean ratio of 4.31 ± 0.10, n = 12, and HFDLS mice had a mean ratio of 4.33 ± 0.06, n = 18. An unpaired two-tailed t-test showed no significant difference (ns, p = 0.877) in pulmonary fluid content between groups. Data are presented as mean ± SEM.

3.4 Assessment of Cardiac Function

Given that HFpEF is characterized by diastolic impairment, concentric LV remodeling, increased arterial pressures, and a high burden of atrial fibrillation, defining the cardiac phenotype requires direct functional assessment. Accordingly, we next evaluated cardiac performance and LV geometry using transthoracic echocardiography, invasive haemodynamics to quantify filling pressures and arterial hypertension, and intracardiac electrophysiology to assess atrial excitability and arrhythmia susceptibility.

3.4.1 Transthoracic Echocardiography

To evaluate LV structure and systolic performance, transthoracic echocardiography was conducted in ND (n = 14) and HFDLS (n = 21) mice (Figure 9A–H; Table 1). All comparisons were analyzed using unpaired two-tailed t-tests. LV systolic diameter (Figure 9A) was significantly reduced in HFDLS mice, measuring 2.747 ± 0.085 mm compared with 3.137 ±

0.096 mm in ND ($p = 0.0053$). LV diastolic diameter (Figure 9B) was also significantly smaller in HFDLS mice, with values of 4.281 ± 0.068 mm versus 4.630 ± 0.084 mm in ND ($p = 0.0026$). Measures of systolic function showed mixed differences between groups. Ejection fraction (Figure 9C) was similar between ND ($60.34 \pm 1.72\%$) and HFDLS mice ($65.42 \pm 1.76\%$; ns, $p = 0.0564$). Fractional shortening (Figure 9E) was significantly increased in the HFDLS cohort, averaging $36.01 \pm 1.35\%$ versus $31.99 \pm 1.25\%$ in ND ($p = 0.0462$). Measures related to ventricular output were unchanged between groups. CO (Figure 9D) was 25.54 ± 1.03 mL/min in HFDLS and 28.91 ± 1.59 mL/min in ND (ns, $p = 0.0701$). Stroke volume (Figure 9G) was similar in HFDLS (53.68 ± 1.85 µL) vs. ND (59.35 ± 2.20 µL; ns, $p = 0.0584$), as was heart rate (Figure 9F), which measured 480 ± 12 bpm in HFDLS compared with 478 ± 18 bpm in ND (ns, $p = 0.9301$). Lastly, LV wall thickness (Figure 9H) was significantly increased in HFDLS mice. ND mice exhibited a mean thickness of 0.9157 ± 0.027 mm, while HFDLS mice measured 1.127 ± 0.025 mm ($p < 0.0001$).

Table 1. Echocardiographic parameters in ND and HFDLS mice.

Parameter	ND (Mean ± SEM)	HFDLS (Mean ± SEM)	p-value	Significance
LV Systolic Diameter	3.137 ± 0.096 mm	2.747 ± 0.085 mm	0.0053	Significant
LV Diastolic Diameter	4.630 ± 0.084 mm	4.281 ± 0.068 mm	0.0026	Significant
Ejection Fraction	60.34 ± 1.72 %	65.42 ± 1.76 %	0.0564	NS
Cardiac Output	28.91 ± 1.59 mL/min	25.54 ± 1.03 mL/min	0.0701	NS
Fractional Shortening	31.99 ± 1.25 %	36.01 ± 1.35 %	0.0462	Significant
Heart Rate	478 ± 18 bpm	480 ± 12 bpm	0.9301	NS
Stroke Volume	59.35 ± 2.20 µL	53.68 ± 1.85 µL	0.0584	NS
LV Wall Thickness	0.9157 ± 0.027 mm	1.127 ± 0.025 mm	<0.0001	Significant
Mean ± SEM values for LV systolic diameter, LV diastolic diameter, ejection fraction, fractional shortening, cardiac output, stroke volume, heart rate, and LV wall thickness were obtained from transthoracic echocardiography (Figure 6A–H). ND (n = 14) and HFDLS (n = 21) groups were compared using unpaired two-tailed Student's t-tests. Significance was defined as $p < 0.05$.				

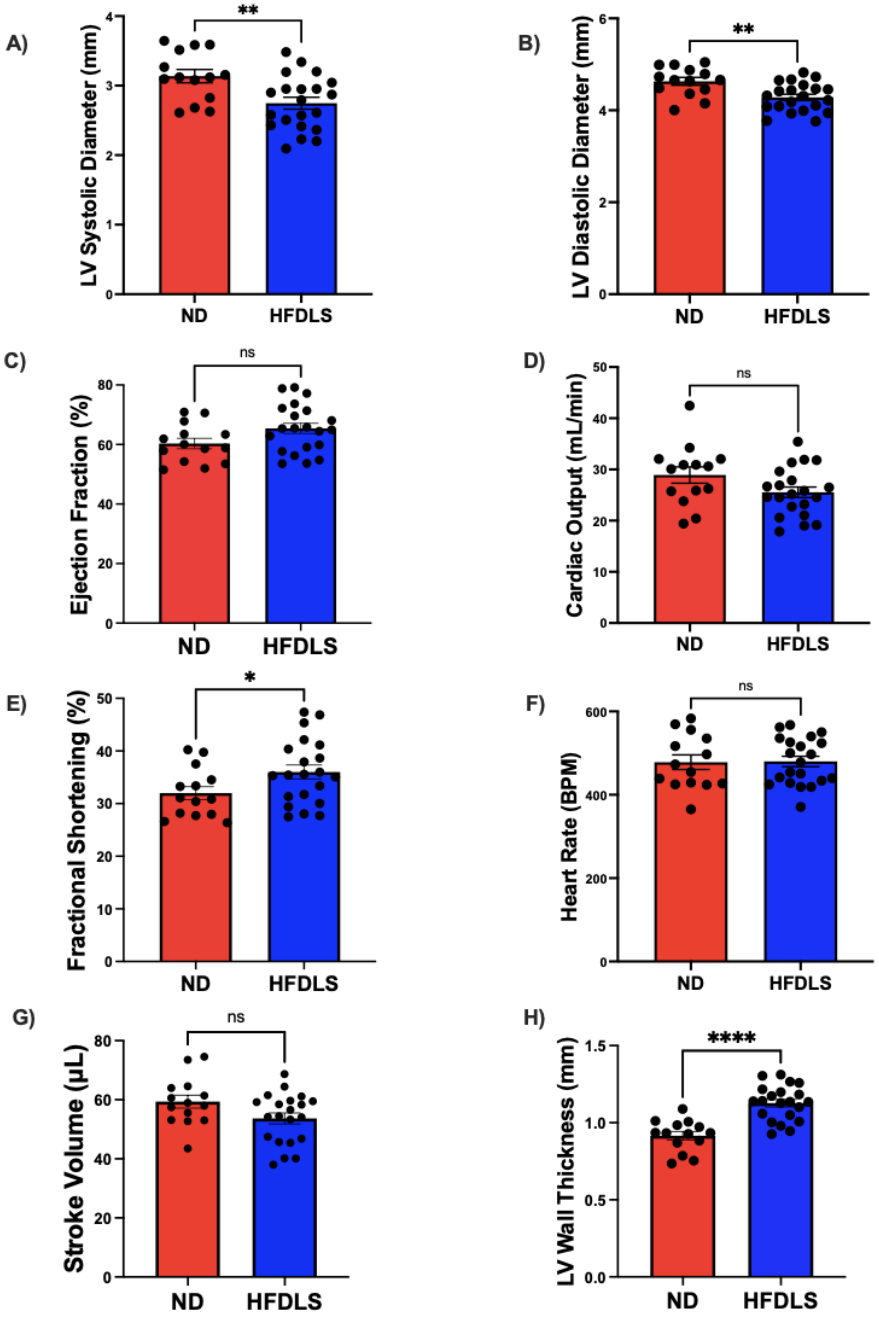

Figure 9. Echocardiographic assessment of left-ventricular structure and systolic function in ND and HFDLS mice. Transthoracic echocardiography was performed as described in Section 2.3 to evaluate LV geometry and systolic performance in ND (n = 14) and HFDLS (n = 21) mice. A) LV systolic diameter was significantly reduced in HFDLS mice compared with ND controls. B) LV diastolic diameter was also significantly decreased in HFDLS mice. C) Ejection fraction did not differ between groups (ns). D) Cardiac output was similar between ND and HFDLS mice (ns). E) Fractional shortening was significantly increased in HFDLS mice. F) Heart rate was unchanged between groups (ns). G) Stroke volume did not differ between diets (ns). H) LV wall thickness was significantly increased in HFDLS mice. Data are presented as mean ± SEM. Statistical comparisons were made using unpaired two-tailed t-tests. Significance levels: $p < 0.05$ (*), $p < 0.01$ (**), $p < 0.0001$ (****); ns = not significant.

3.4.2 Invasive Haemodynamics

Arterial pressure measurements (Figure 10; Table 2) were obtained in ND (n = 14) and HFDLS (n = 20) mice using the invasive hemodynamic procedure described in Section 2.6. Systolic blood pressure (SBP) was significantly elevated in HFDLS mice (134.2 ± 2.81 mmHg) compared with ND controls (104.6 ± 2.86 mmHg; $p < 0.0001$, unpaired two-tailed t-test with Welch's correction). Diastolic blood pressure (DBP) was also significantly higher in HFDLS mice (95.16 ± 1.55 mmHg) relative to ND (72.82 ± 2.70 mmHg; $p < 0.0001$). Mean arterial pressure (MAP) followed the same pattern, with HFDLS exhibiting markedly increased values (108.2 ± 1.74 mmHg) compared with ND (83.42 ± 2.70 mmHg; $p < 0.0001$). HFDLS mice exhibited significantly higher values across all three arterial pressure measurements, indicating a robust hypertensive phenotype.

Table 2. Arterial Blood Pressure Measurements in ND and HFDLS Mice.

Parameter	ND (Mean ± SEM)	HFDLS (Mean ± SEM)	p-value	Significance
SBP	104.6 ± 2.856 mmHg	134.2 ± 2.805 mmHg	<0.0001	Significant
DBP	72.82 ± 2.702 mmHg	95.16 ± 1.549 mmHg	<0.0001	Significant
MAP	83.42 ± 2.700 mmHg	108.2 ± 1.743 mmHg	<0.0001	Significant
Systolic blood pressure (SBP), diastolic blood pressure (DBP), and mean arterial pressure (MAP) were recorded using a Millar catheter inserted into the right carotid artery under isoflurane anesthesia (see Section 2.6). Values represent mean ± SEM for ND (n = 14) and HFDLS (n = 20) mice. Statistical comparisons between groups were performed using unpaired two-tailed Welch's t-tests.				

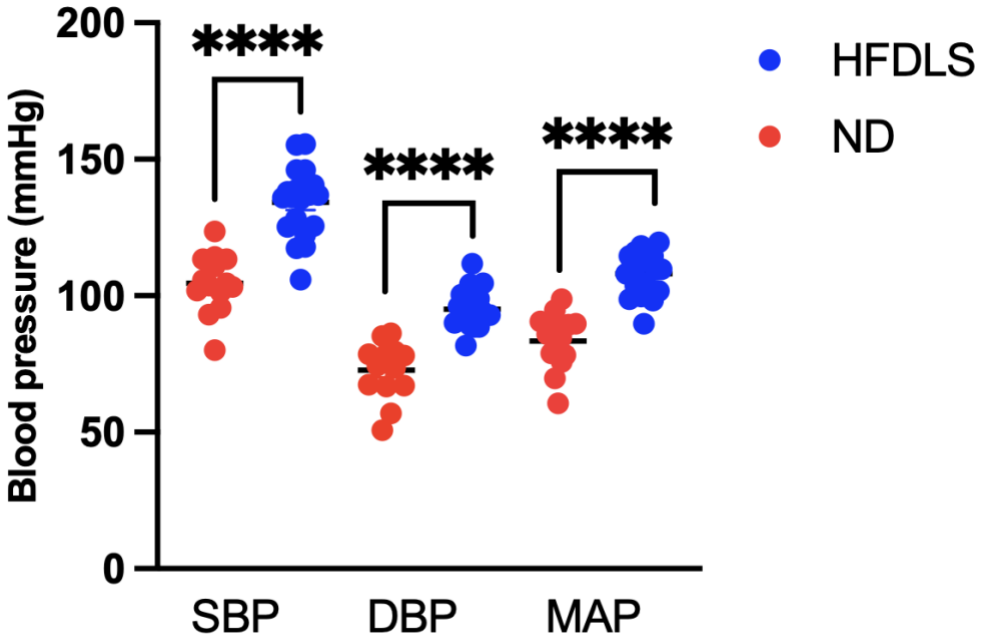

Figure 10. Arterial blood pressure measurements in ND and HFDLS mice. Systolic blood pressure (SBP), diastolic blood pressure (DBP), and mean arterial pressure (MAP) were measured using invasive arterial catheterization during hemodynamic assessments (Section 2.6). HFDLS (n = 20) mice consistently exhibited higher pressures across all three parameters compared with ND (n = 14) controls. SBP, DBP, and MAP were each significantly elevated in HFDLS mice (unpaired two-tailed t-tests with Welch's correction; SBP: $p < 0.0001$; DBP: $p < 0.0001$; MAP: $p < 0.0001$). Data are presented as individual mice with mean ± SEM. $p < 0.0001$ (****).

Invasive hemodynamic recordings were performed in ND (n = 14) and HFDLS (n = 20) mice to evaluate LV systolic and diastolic pressures, as well as pressure generation and relaxation (Figure 11A–D; Table 3). End-systolic pressure (ESP) was significantly elevated in HFDLS mice, averaging 116.2 ± 3.316 mmHg compared with 96.31 ± 1.822 mmHg in ND controls ($p < 0.0001$; unpaired two-tailed t-test with Welch's correction) (Figure 11A). End-diastolic pressure (EDP) was slightly higher in HFDLS mice (9.086 ± 1.327 mmHg) relative to ND (6.825 ± 0.790 mmHg), although this difference did not reach significance (ns, $p = 0.1539$) (Figure 11B). Maximal contractile pressure development (Max dP/dt) was significantly increased in the HFDLS group, measuring 10,969 ± 297.4 mmHg/s versus 9,989 ± 301.6 mmHg/s in ND ($p = 0.0276$) (Figure 11C). Minimal dP/dt, an index of LV relaxation, was also significantly more negative in HFDLS mice (–10,172 ± 298.1 mmHg/s) compared with ND controls (–9,120 ± 243.1 mmHg/s; $p = 0.0101$) (Figure 11D).

Table 3. Left-ventricular hemodynamic parameters in ND and HFDLS mice.

Parameter	ND (Mean ± SEM)	HFDLS (Mean ± SEM)	p-value	Significance
End-Systolic Pressure	96.31 ± 1.822 mmHg	116.2 ± 3.316 mmHg	<0.0001	Significant
End-Diastolic Pressure	6.825 ± 0.7902 mmHg	9.086 ± 1.327 mmHg	0.1539	NS
Maximum dP/dt	9989 ± 301.6 mmHg/s	10969 ± 297.4 mmHg/s	0.0276	Significant
Minimum dP/dt	-9120 ± 243.1 mmHg/s	-10172 ± 298.1 mmHg/s	0.0101	Significant
End-systolic pressure (ESP), end-diastolic pressure (EDP), and indices of systolic (max dP/dt) and diastolic (min dP/dt) function were obtained by invasive pressure–volume recordings as described in Section 2.6. Data are presented as mean ± SEM for ND (n = 14) and HFDLS (n = 20) groups. Statistical comparisons were performed using unpaired two-tailed Welch's t-tests. Significant differences ($p < 0.05$) are indicated.				

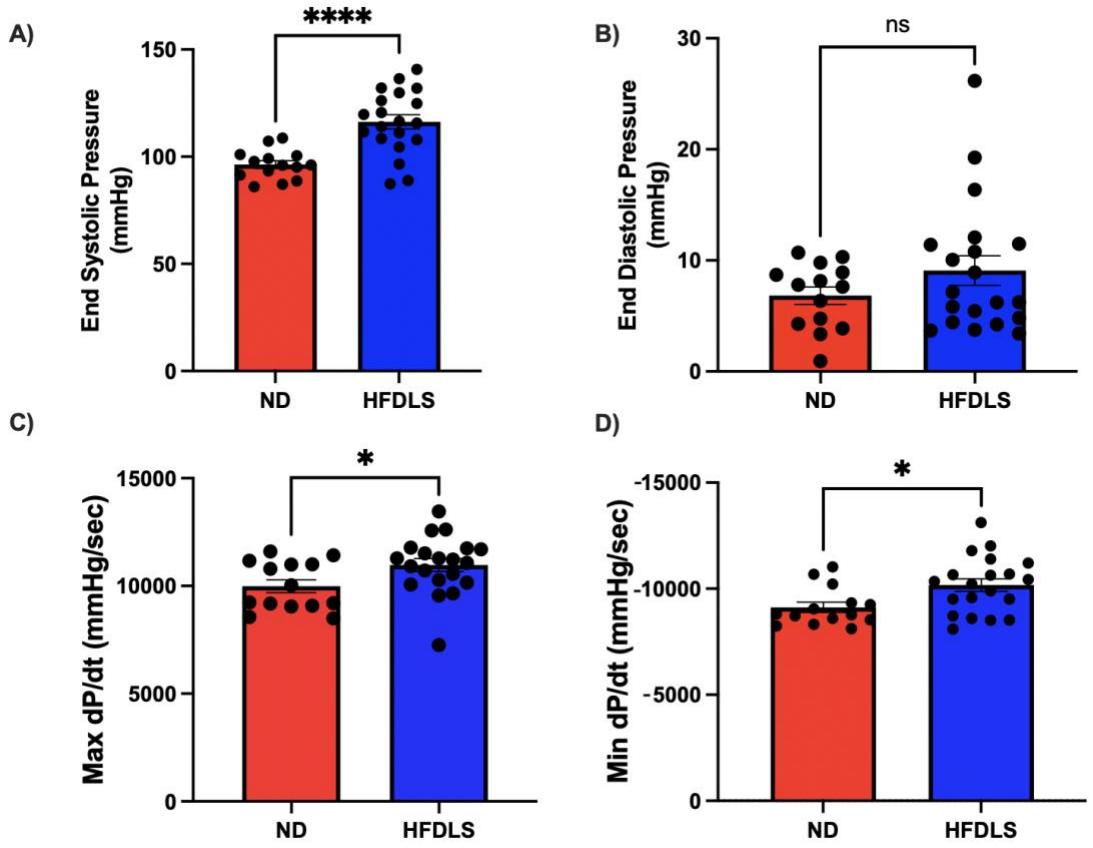

Figure 11. Invasive left-ventricular hemodynamic assessment in ND and HFDLS mice. Invasive LV pressure measurements were performed as described in Section 2.6 to evaluate systolic and diastolic pressures, as well as contractility and relaxation, in normal diet (ND; n = 14) and high-fat, L-NAME, sucrose (HFDLS; n = 20) mice. A) End-systolic pressure (ESP) was significantly higher in HFDLS mice compared with ND controls. B) End-diastolic pressure (EDP) did not differ significantly between groups (ns), although values showed a modest upward trend in HFDLS mice. C) Maximum dP/dt, an index of contractile performance, was significantly increased in HFDLS mice. D) Minimum dP/dt, reflecting peak relaxation rate, was significantly more negative in HFDLS mice. Data are presented as mean ± SEM. Statistical comparisons were performed using unpaired two-tailed t-tests, with Welch's correction applied when required ($\alpha = 0.05$). Significance levels: $p < 0.05$ (*), $p < 0.01$ (**) $p < 0.0001$ (****); ns = not significant.

3.4.3 Intracardiac Electrophysiology

To assess electrical remodeling in the HFpEF model, intracardiac electrophysiology (Figure 12) was performed in ND (n = 14) and HFDLS (n = 21) mice. Atrial effective refractory period (AERP) did not differ between groups, with ND mice exhibiting 26.93 ± 0.92 ms and HFDLS mice 25.33 ± 0.42 ms (Figure 12A). Because variances were unequal, this comparison was evaluated using an unpaired two-tailed t-test with Welch's correction, which indicated no significant difference (ns, $p = 0.13$). Atrioventricular effective refractory period (AVERP) was also similar between ND (50.50 ± 0.88 ms) and HFDLS (48.71 ± 0.97 ms) mice (Figure 12B), assessed using an unpaired two-tailed t-test (ns, $p = 0.21$). Ventricular effective refractory period (VERP) remained unchanged, with ND at 29.00 ± 0.90 ms and HFDLS at 29.86 ± 0.91 ms (Figure 12C), assessed using an unpaired two-tailed t-test (ns, $p = 0.53$), indicating preserved baseline atrial and ventricular excitability in the HFpEF cohort.

In contrast, atrial arrhythmia duration was substantially prolonged in HFDLS mice, which displayed 23.60 ± 8.26 s compared with 2.61 ± 1.58 s in ND controls (Figure 12D). Because the data did not meet normality assumptions, this comparison was assessed using a Mann–Whitney U test, confirming a significant increase ($p = 0.0097$). Ventricular arrhythmia duration remained minimal across groups, with ND mice showing 0.28 ± 0.13 s and HFDLS mice 2.64 ± 1.12 s (Figure 12E). This comparison was evaluated using a Mann–Whitney U test and was not statistically significant (ns, $p = 0.38$), although HFDLS mice exhibited a modest upward trend toward greater durations. Collectively, these findings demonstrate that while atrial and ventricular refractoriness remain unchanged, HFD + L-NAME + sucrose induces increased atrial electrical vulnerability characterized by prolonged arrhythmia duration, with no evidence of increased ventricular arrhythmogenicity.

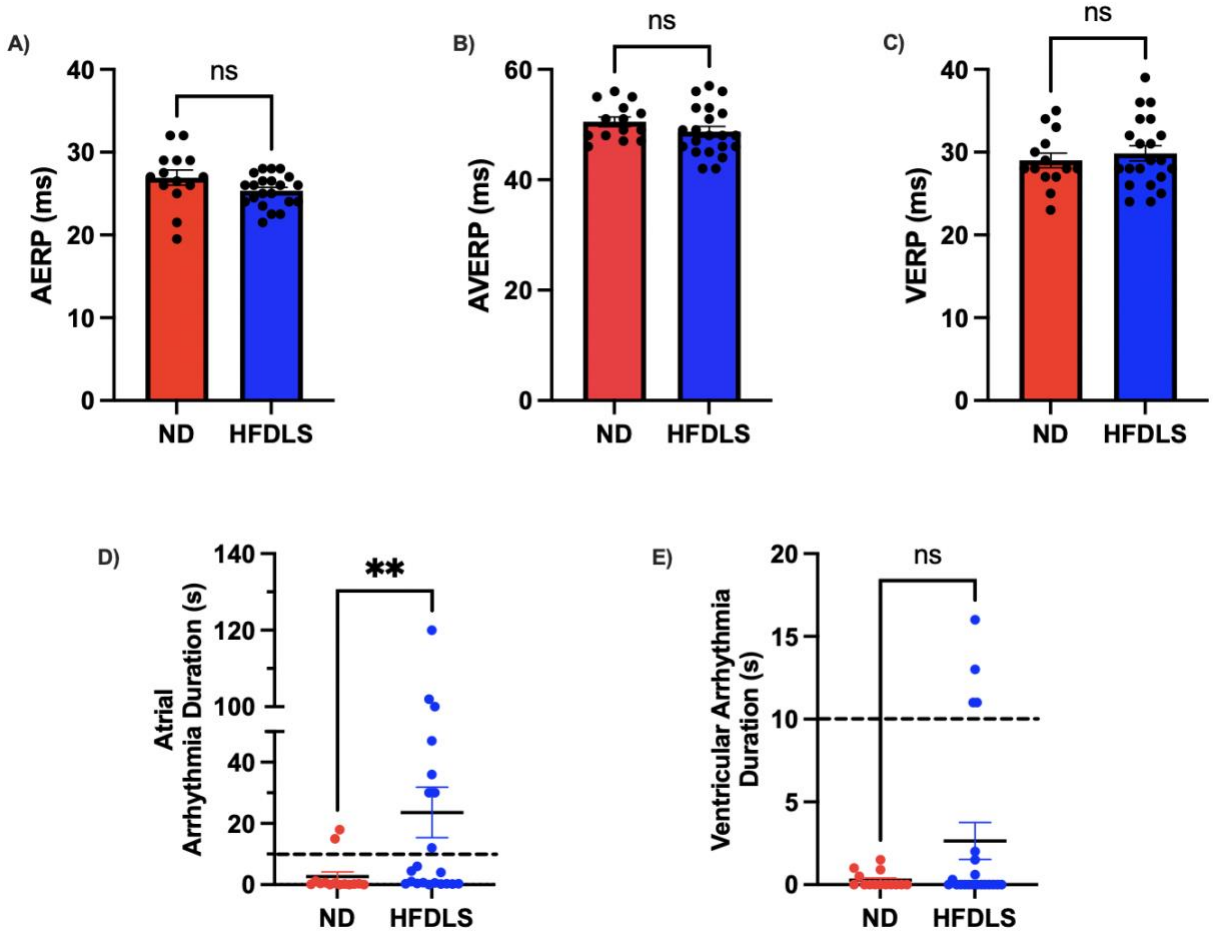

Figure 12. Intracardiac electrophysiology demonstrates preserved refractoriness with increased arrhythmia vulnerability in HFDLS mice. Intracardiac electrophysiology was performed as described in Section 2.5 to evaluate atrial and ventricular refractoriness, as well as arrhythmia vulnerability, in ND (n = 14) and HFDLS (n = 21) mice. A) Atrial effective refractory period (AERP) did not differ significantly between groups (ns). B) Atrioventricular effective refractory period (AVERP) was similar between ND and HFDLS mice (ns). C) Ventricular effective refractory period (VERP) also remained comparable across groups (ns). D) Atrial arrhythmia duration was significantly increased in HFDLS mice ($p = 0.0097$). E) Ventricular arrhythmia duration remained low in both groups (ns), although HFDLS mice showed a modest upward trend. Data are presented as mean ± SEM. Statistical comparisons were performed using an unpaired two-tailed t-test with Welch's correction for AERP, unpaired two-tailed t-tests for AVERP and VERP, and Mann–Whitney U tests for atrial and ventricular arrhythmia duration. Significance levels: $p < 0.01$ (**); ns = not significant.

3.5 Histopathological and Immunohistochemical Characterization

Having established the functional, metabolic, and electrophysiological abnormalities characteristic of the HFpEF phenotype, we next examined the underlying tissue-level changes through histopathological and immunohistochemical analyses, specifically assessing myocardial fibrosis using Picrosirius Red staining and evaluating immune-cell infiltration using macrophage markers.

3.5.1 Assessment of Myocardial Fibrosis via Picrosirius Red Staining

Myocardial fibrosis was significantly increased in HFDLS mice compared with ND controls (Figure 13A–F). In the left atrium, ND mice exhibited 5.96 ± 0.51% fibrosis (n = 12), whereas HFDLS mice displayed 12.15 ± 1.12% (n = 16) (Mann–Whitney test, $p = 0.0003$) (Figure 10A). LV collagen content showed a similar pattern, with ND mice exhibiting 1.71 ± 0.19% and HFDLS mice exhibiting 3.76 ± 0.32% (Welch's t-test, $p < 0.0001$) (Figure 13B). Representative Picrosirius Red–stained sections illustrate atrial collagen in ND (Figure 14A) and HFDLS (Figure 14B) mice, and ventricular collagen in ND (Figure 13C) and HFDLS (Figure 14D), confirming the quantitative increase in fibrosis.

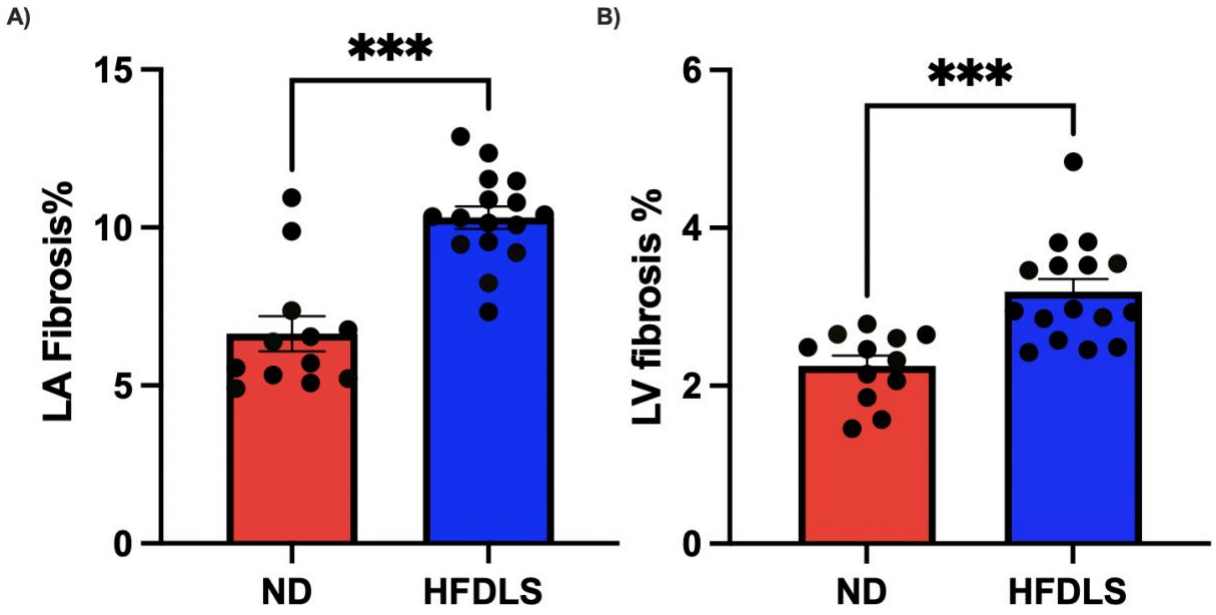

Figure 13. Myocardial fibrosis is significantly increased in HFDLS mice. Myocardial collagen content was quantified in normal diet (ND) and high-fat, L-NAME, sucrose (HFDLS) mice using Picrosirius Red staining. A) Left-atrial (LA) fibrosis was significantly higher in HFDLS mice compared with ND. ND mice exhibited 5.96 ± 0.51% fibrosis (n = 12), whereas HFDLS mice exhibited 12.15 ± 1.12% (n = 16) (Mann–Whitney test, $p = 0.0003$). B) Left-ventricular (LV) fibrosis was also significantly increased in HFDLS mice. ND mice exhibited 1.71 ± 0.19% fibrosis (n = 12), whereas HFDLS mice exhibited 3.76 ± 0.32% (n = 16) (Welch's unpaired t-test, $p < 0.0001$). Data are presented as mean ± SEM. Significance levels: ***$p < 0.001$, ****$p < 0.0001$.

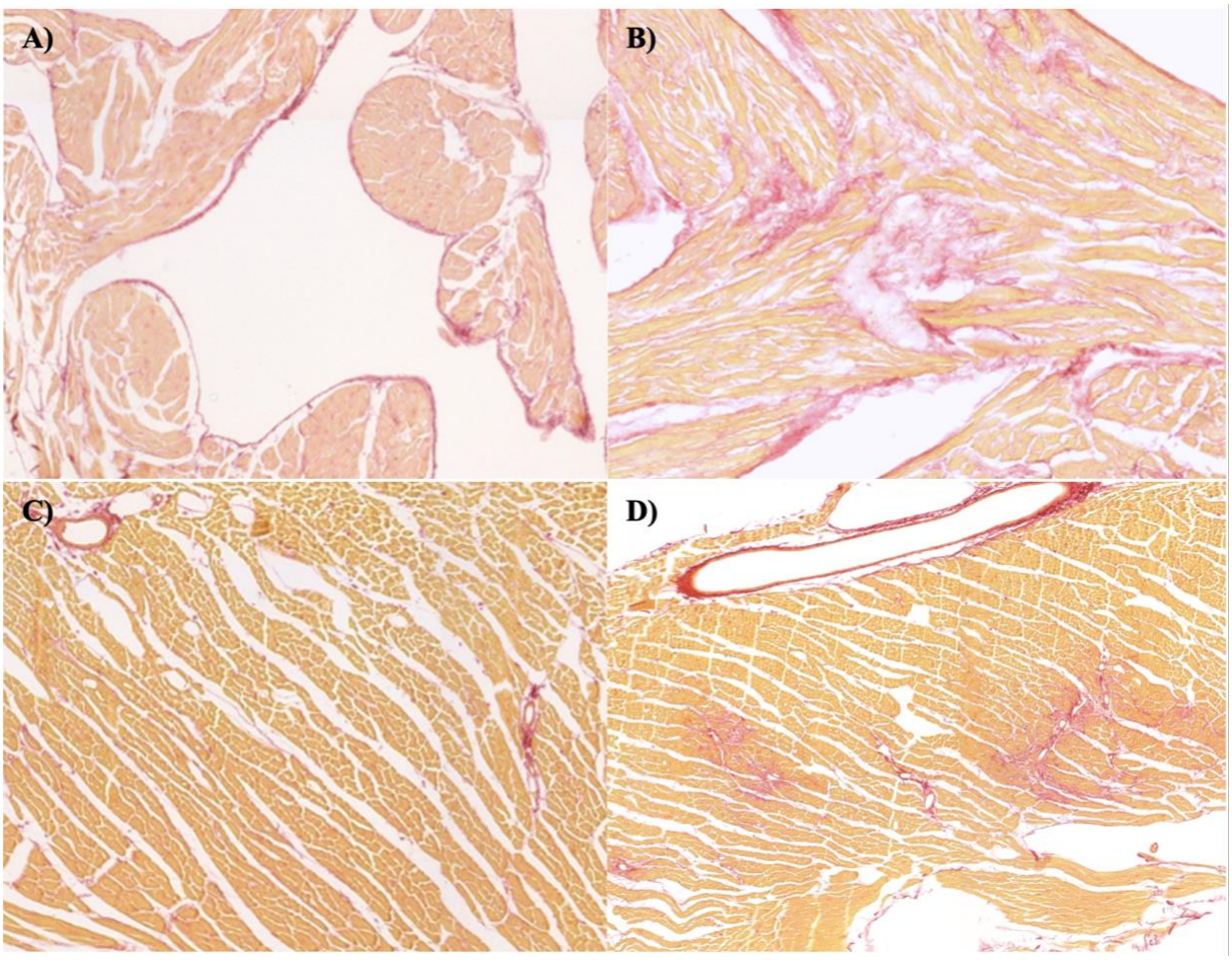

Figure 14. Representative Picrosirius Red–stained images demonstrating increased myocardial fibrosis in HFDLS mice. Picrosirius Red staining was performed to visualize extracellular matrix collagen in the left atrial appendage (LAA) and left ventricle (LV) of normal diet (ND) and high-fat, L-NAME, sucrose (HFDLS) mice. Representative sections show LA collagen in A) ND and B) HFDLS mice, and LV collagen in C) ND and D) HFDLS mice. These images correspond to the quantitative fibrosis measurements presented in Figure 10A–B.

3.5.2 Immunohistological Analysis

Preliminary immunohistochemical analyses were performed to quantify inflammatory cell infiltration in atrial and ventricular tissue from ND and HFDLS mice. $F4/80^+$ staining was used to identify cardiac-resident macrophages, which represent the predominant macrophage population in the myocardium. In the LAA, ND mice exhibited 623.5 ± 50.64 cells/mm² ($n = 3$), whereas HFDLS mice showed 842.7 ± 55.21 cells/mm² ($n = 5$) (unpaired two-tailed t-test, $p < 0.05$), indicating increased macrophage density in HFDLS mice (Figure 15A). A similar pattern was observed in the LV, where ND mice displayed 781.1 ± 81.67 cells/mm² ($n = 3$) compared with 1291.0 ± 97.37 cells/mm² ($n = 4$) in HFDLS mice (unpaired two-tailed t-test, $p < 0.05$) (Figure 15B). Representative images (figure 16) illustrate that the signal intensity is notably greater in the HFDLS group. To further assess inflammatory cell subtypes, present in the myocardium, CCR2 immunostaining was also performed to identify recruited monocyte-derived macrophages; however, staining consistency and signal specificity were suboptimal, and additional optimization will be required before quantitative analysis can be reliably completed. Collectively, these preliminary data suggest enhanced macrophage-driven inflammatory remodeling in both the atrial and ventricular compartments of HFDLS mice.

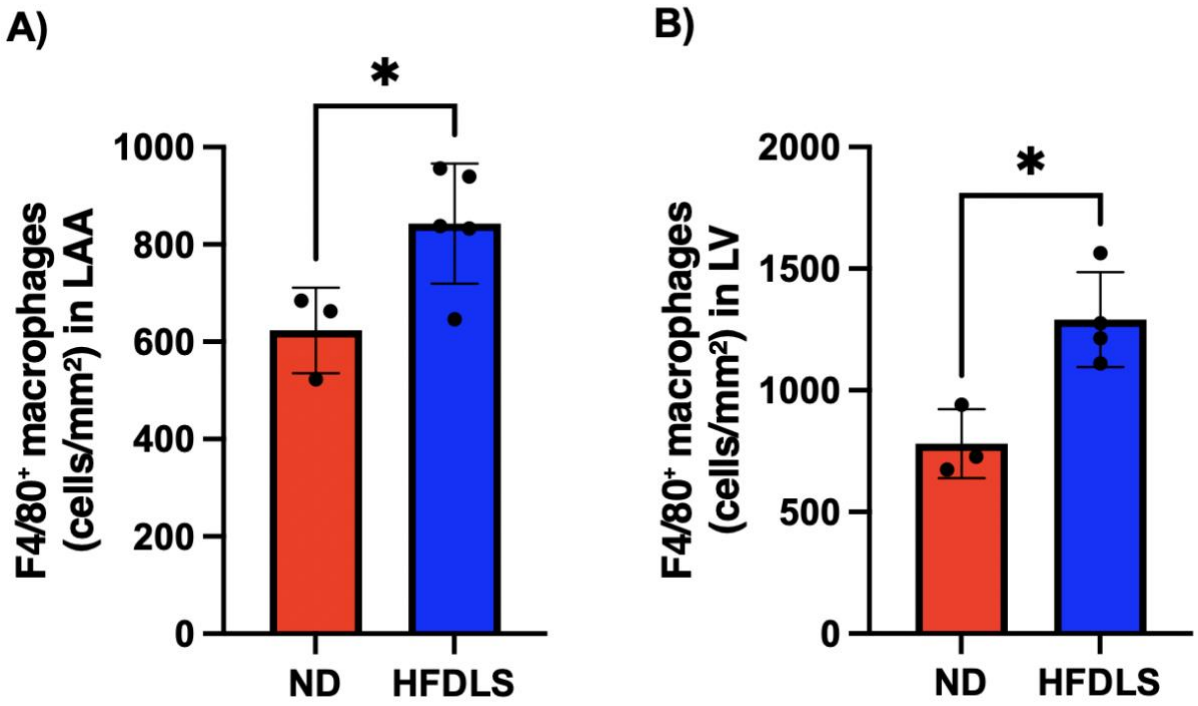

Figure 15. Preliminary immunohistochemical assessment of cardiac-resident F4/80⁺ macrophages in ND and HFDLS mice. F4/80⁺ macrophage density was quantified in the left atrial appendage (LAA) and left ventricle (LV) to evaluate immune-cell remodeling. A) LAA F4/80⁺ macrophage density was significantly increased in HFDLS mice compared with ND controls. ND mice exhibited 623.5 ± 50.64 cells/mm² (n = 3), whereas HFDLS mice exhibited 842.7 ± 55.21 cells/mm² (n = 5) (unpaired two-tailed t-test, p = 0.032). B) LV F4/80⁺ macrophage density was also significantly higher in HFDLS mice. ND mice showed 781.1 ± 81 cells/mm² (n = 4), and HFDLS mice showed 1291.0 ± 97.37 cells/mm² (n = 4) (unpaired two-tailed t-test, p = 0.028).

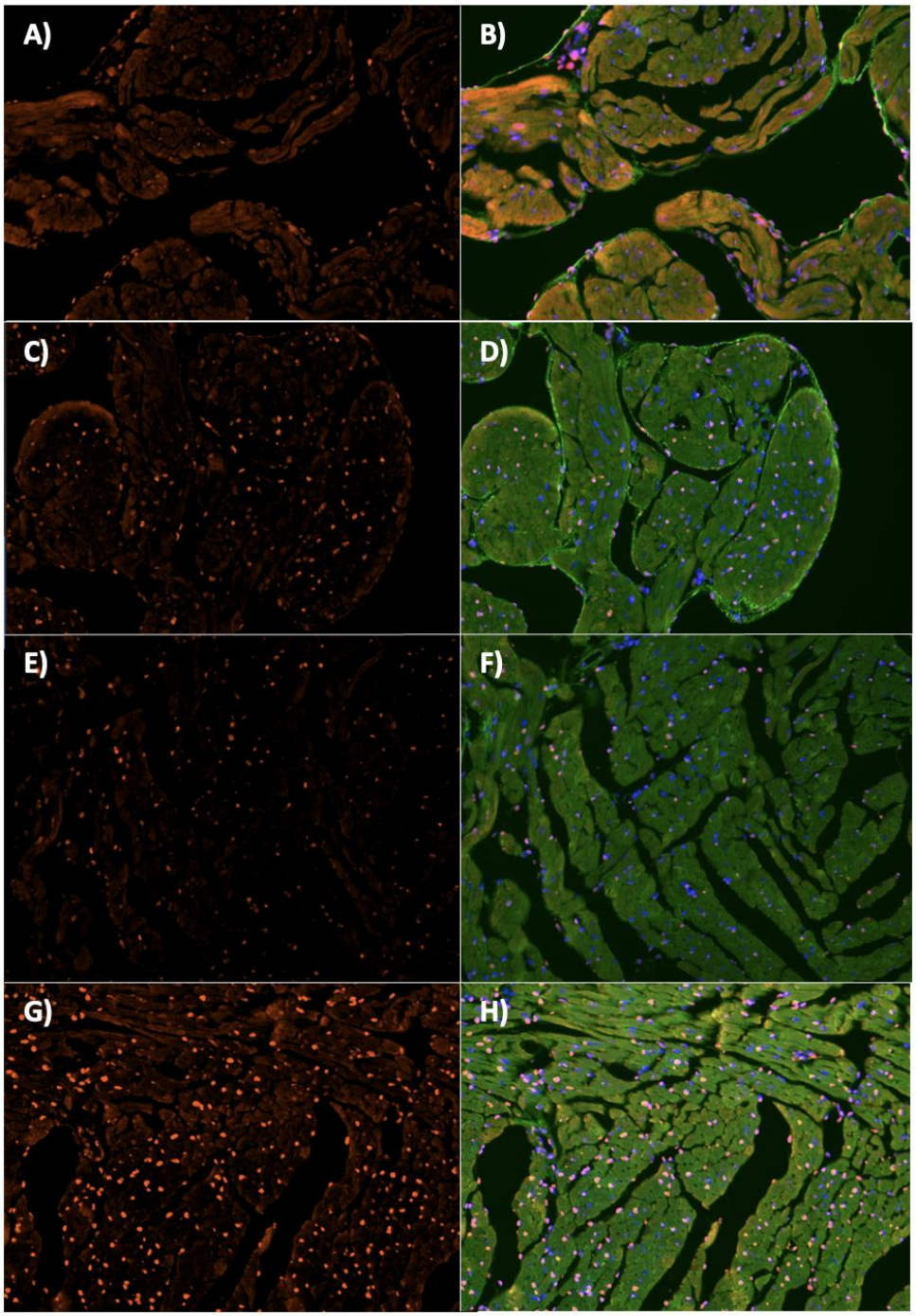

Figure 16. Representative immunofluorescent images of F4/80$^+$ cardiac macrophages in the left atrial appendage (LAA) and left ventricle (LV) of ND and HFDLS mice. A) ND LAA – F4/80$^+$ macrophages (orange) shown alone. B) ND LAA – F4/80$^+$ signal overlaid with WGA (green) and DAPI (blue). C) HFDLS LAA – F4/80$^+$ macrophages shown alone. D) HFDLS LAA – F4/80$^+$ signal overlaid with WGA and DAPI. E) ND LV – F4/80$^+$ macrophages shown alone. F) ND LV – F4/80$^+$ signal overlaid with WGA and DAPI. G) HFDLS LV – F4/80$^+$ macrophages shown alone. H) HFDLS LV – F4/80$^+$ signal overlaid with WGA and DAPI. Images were acquired for qualitative visualization of cardiac-resident macrophage distribution and morphology in atrial and ventricular tissue.

Chapter 4: Discussion

The primary objective of this study was to establish and comprehensively characterize a murine model of HFpEF using combined high-fat feeding along with L-NAME administration in the CD1 mouse strain. This approach is novel because HFD and L-NAME have never been used to induce HFpEF in CD1 mice, and the physiological response of this strain to these combined stressors was unknown. The initial plan was to replicate a previously published HFpEF murine model utilizing HFD and L-NAME, which has been characterized in other mouse strains[26,42]. In CD1 mice, however, this combination produced a weak and inconsistent HFpEF phenotype. As a result, an extended optimization period was required. Based on prior studies showing that sucrose supplementation exacerbates metabolic dysfunction, hypertension, and cardiac impairment when added to high-fat feeding, sucrose was incorporated to intensify the metabolic and cardiovascular burden[64,65,154]. Different concentrations of L-NAME and sucrose were then tested, along with HFD feeding, across several cohorts to determine the combination capable of reliably producing a stable phenotype. This refinement period required substantial time and limited the ability to proceed to the subsequent objectives involving pharmacological TNFα inhibition and TNFα knockout models. Developing a reliable model in CD1 mice is clinically and scientifically relevant because HFpEF is highly heterogeneous across patient populations and understanding how different genetic backgrounds respond to cardiometabolic stressors helps improve the translational relevance of preclinical models.

Following optimization, the refined protocol successfully produced several hallmark features of HFpEF, including evidence of impaired diastolic relaxation, along with metabolic dysfunction, reduced exercise tolerance, arterial hypertension, concentric remodelling, increased atrial and ventricular fibrosis, along with preliminary results indicating increased expansion of cardiac-resident macrophage populations. Chamber-specific analyses revealed that the atria exhibited disproportionately greater remodeling relative to the ventricle, reflected by increased fibrosis, electrophysiological alterations, and inflammatory activation. The results of this study indicated that the LAA had higher collagen deposition than the ventricle, consistent with more pronounced electrical remodeling. HFDLS mice also showed a trend towards a decreased AERP and a marked increase in AF inducibility, while ventricular arrhythmia susceptibility did not increase, indicating that electrical instability was confined to the atria. Preliminary

immunohistochemical analyses further support this chamber-specific inflammatory response, as $F4/80^+$ macrophage staining demonstrated increased macrophage density in both the left atrial appendage and left ventricular free wall, with a more pronounced elevation observed in the LV. Although these macrophage data are preliminary, they align with the observed electrophysiological vulnerability and greater collagen accumulation, suggesting that inflammatory activation may contribute disproportionately to atrial remodeling in this model. These preliminary findings are also consistent with reports showing increased macrophage presence in the HFpEF myocardium, particularly in cardiometabolic models in which cardiac-resident macrophage populations expand[155,156].

Establishing these chamber-dependent differences provides the foundation needed to test the second hypothesis that TNFα acts as the upstream driver of the divergent remodeling patterns observed between the atria and ventricles. The successful characterization of this model provides the essential platform required for future studies designed to determine how TNFα signaling influences myocardial remodeling, susceptibility to arrhythmia in HFpEF, vascular tone, and nitrosative stress.

4.1 Metabolic Findings

The dietary intervention produced a clear and sustained metabolic shift in CD1 mice, most prominently reflected by the substantial increase in body weight observed throughout the study. This confirms that the combination of high-fat feeding and sucrose supplementation generated sufficient metabolic burden, despite the relative resistance of CD1 mice to diet-induced metabolic disturbances[157]. Despite this significant weight gain, alterations in glucose handling were modest. HFDLS mice exhibited higher circulating glucose levels during the glucose tolerance test, but these differences did not reach statistical significance, indicating that overt glucose intolerance did not fully develop under the conditions used. Prior work has shown that long-term exposure to high-fat and high-sucrose diets can initially impair glucose tolerance but may later lead to a partial normalization as animals adapt to chronic nutrient excess[158,159]. Given the extended duration of feeding in this study, such adaptive responses may have contributed to the relatively mild differences observed in glycemic regulation. Future studies

incorporating earlier metabolic assessments would help determine when glucose intolerance first emerges and whether it later stabilizes in this model.

In contrast to the mild glycemic phenotype, HFDLS mice displayed a marked reduction in voluntary running distance, indicating impaired exercise tolerance. While the present study did not assess hemodynamic responses during exercise, HFpEF is characterized by an impaired ability to maintain low filling pressures under physiological stress known as reduced diastolic reserve[159]. In clinical HFpEF, exercise intolerance arises when the heart fails to accommodate increased venous return without a disproportionate rise in LV and LA pressures[160]. While exercise-induced changes in filling pressures were not measured in this study, the presence of increased body weight gain, hypertension, and indicators of diastolic impairment suggests that HFDLS mice operated with reduced physiological reserve. In this context, the decline in exercise tolerance is best interpreted as a consequence of the combined metabolic and cardiovascular burden generated by the intervention.

Together, these findings demonstrate that the intervention successfully established a systemic environment conducive to HFpEF development. These metabolic and physiological effects establish the conditions that contribute to the cardiac remodeling described in the next section.

4.2 Cardiac Structural and Functional Findings

The cardiac phenotype observed in this model reflects several hallmark features of HFpEF. CD1 mice developed arterial hypertension along with evidence of concentric remodelling, indicating an adaptive response to increased vascular load[161]. Although heart weight was not significantly increased, prior studies have shown that concentric remodeling can occur with elevated relative wall thickness despite a normal LV mass, representing an early adaptive response to increased blood pressure[162,163]. Atrial and ventricular fibrosis were also significantly elevated, which is consistent with pressure-overload driven structural remodeling found in HFpEF[49]. Importantly, ejection fraction remained preserved, consistent with the defining criteria of HFpEF, and confirmed that systolic function was maintained despite substantial structural changes. Diastolic function was assessed through invasive hemodynamics, which demonstrated an upward trend in LV EDP in HFDLS mice. Although not statistically significant, the direction

of change suggests the presence of early impairments in diastolic filling. In both HFpEF animal models and clinical HFpEF, filling pressures often remain near normal at rest, with pathological elevations becoming obvious during physiological or pharmacological stress[159,164]. The absence of a significant increase in LV EDP at rest in this study could reflect the limitations of baseline measurements rather than a true absence of diastolic impairment. This is supported by the presence of hypertension, structural remodeling, and reduced exercise tolerance in HFDLS mice, which together indicate impaired cardiac reserve.

Consistent with the modest elevation in resting diastolic filling pressures, the assessment of pulmonary congestion did not reveal differences between groups. This aligns with the understanding that pulmonary fluid accumulation in HFpEF often emerges during periods of increased hemodynamic demand, such as exercise, rather than under resting conditions. Taken together, the combination of preserved systolic function, early diastolic abnormalities, hypertension, and structural remodeling indicates that this model successfully reproduced the central cardiac features characteristic of HFpEF.

4.3 Chamber-Specific Remodelling and Electrophysiological Vulnerability

A clear chamber specific pattern of remodelling emerged in this model, with the atria showing a greater degree of structural and electrical vulnerability than the ventricles. Although both chambers displayed significantly increased fibrosis, it was far more pronounced in the atria. This aligns with clinical and experimental observations that the atria are more sensitive to pressure and metabolic stress in HFpEF, and experience earlier and more extensive structural remodeling than the ventricles[106,165]. Increased atrial fibrosis reduces compliance and promotes conduction heterogeneity, which together create a substrate that facilitates arrhythmia development[25,166,167].

This chamber-specific pattern was also evident in the electrophysiological assessments. HFDLS mice exhibited a trend toward reduced AERP, indicating increased atrial excitability. HFDLS mice had a marked increase in atrial arrhythmia duration, indicating greater atrial electrical vulnerability, while ventricular arrhythmia susceptibility did not differ. The combination of increased atrial fibrosis, trend toward reduced refractoriness, and enhanced AF

vulnerability suggests that the atria are disproportionately affected in this model, while the ventricles remain relatively stable from an electrical standpoint.

These findings align with the high burden of AF observed in patients with HFpEF, where atrial remodeling often precedes or accompanies ventricular changes[168]. The increased vulnerability of the atria in this model supports the first hypothesis of this thesis, which proposed that HFpEF induction would produce distinct remodeling patterns in the atria and ventricles, and that these atrial specific changes would contribute to an increased susceptibility to arrhythmia. This section also establishes the foundation for interpreting the inflammatory findings discussed next, since inflammation is known to interact with both structural and electrical remodeling in a chamber specific manner[25,33,148].

4.4 Inflammation and Macrophage Findings

Preliminary immunohistochemical analysis revealed significantly increased F4/80$^+$ macrophage density in both the atria and ventricles of HFDLS mice. Although this was based on F4/80 staining alone and included a small sample size, the overall pattern is consistent with studies showing that HFpEF is accompanied by enhanced myocardial inflammation, including expansion of resident cardiac macrophage populations[155,156]. The increase in macrophage density in HFDLS mice is likely related to the combined metabolic and hemodynamic stress present in the model[169,170].

Macrophages are known to interact closely with both fibroblasts and myocytes, and increased macrophage presence has been associated with greater tissue remodeling in several preclinical HFpEF models[38,171,172]. In this study, macrophage accumulation was increased in both the LA and LV, which is consistent with the increased fibrosis observed in both chambers. However, the functional implications of macrophage expansion appear to differ between chambers. In the atria, macrophage accumulation has been specifically linked to enhanced fibrosis, conduction abnormalities, and a greater propensity for arrhythmia, which aligns with the chamber specific remodeling and the increased atrial arrhythmia duration observed in this model[173]. Although ventricular arrhythmias have been described in HFpEF, their mechanisms are less clearly defined, and no differences in ventricular arrhythmia susceptibility were observed in

this study[174]. This suggests that the functional consequences of macrophage expansion in this model are more prominent in the atria than in the ventricles.

These findings also relate directly to the second hypothesis of this thesis, which proposes that TNFα contributes to chamber-specific remodelling in HFpEF. TNFα is a well-established upstream inflammatory cytokine that promotes macrophage recruitment, activation, and survival within cardiac tissue[146]. Although TNFα itself was not measured in the present study, the increased macrophage accumulation observed in both the atria and the ventricles provides preliminary support for future experiments evaluating whether TNFα drives the differential remodelling patterns identified in this model. Additional work combining direct assessment of TNFα expression, broader inflammatory markers, and co-staining approaches across larger cohorts will be necessary to clarify the specific inflammatory pathways involved and determine how TNFα influences atrial and ventricular remodeling in HFpEF.

Together, these findings indicate that inflammatory processes are present in this model and may contribute to the structural and electrical changes described above. The following section outlines the key limitations of the study and identifies the most important directions for future work.

4.5 Limitations and Future Directions

While this model reproduced several characteristics of HFpEF, important limitations remain that influence how the findings should be interpreted. Addressing these limitations will help guide the next steps in optimizing the model and designing future experiments.

4.5.1 Limitations

Several limitations should be considered when interpreting the findings from this study. First, although the intervention reproduced multiple characteristics of HFpEF, the overall phenotype was modest. Several features emerged as trends rather than statistically significant differences, particularly those related to diastolic function, pulmonary congestion, and the increase in heart weight, which is the most direct measure of cardiac hypertrophy. HFpEF is known to exhibit more pronounced abnormalities under physiological stress, and because this

study assessed hemodynamics only at rest, the severity of diastolic dysfunction may not have been fully captured. Additionally, diastolic function was not assessed using tissue Doppler imaging, which is commonly used in both clinical and preclinical HFpEF studies to identify impaired relaxation and elevated filling pressures[2]. The absence of tissue Doppler–derived parameters limit the ability to confirm diastolic dysfunction using parameters that are widely reported in the HFpEF literature. When compared with established cardiometabolic HFpEF models outlined in Daou et al. (2025), the current model reproduced several key domains such as hypertension, left ventricular hypertrophy, fibrosis, preserved ejection fraction, and reduced exercise tolerance, but did not robustly capture others[26]. Notably, the model did not develop clear glucose intolerance, did not show measurable pulmonary edema at rest, and did not include left atrial enlargement assessment, which are key criteria used to score the fidelity of HFpEF models in preclinical evaluation. As a result, while the model successfully induced important features of cardiometabolic HFpEF, it demonstrates a more modest phenotype relative to higher scoring models, and certain HFpEF domains were either absent, incompletely assessed, or did not fully meet the criteria[26].

A second limitation relates to how pulmonary congestion was assessed. Although lung wet-to-dry ratios were measured, this approach is relatively insensitive for detecting mild, intermittent, or exercise-induced pulmonary congestion that is characteristic of HFpEF[175,176]. Wet-to-dry ratios quantify total lung water at a single terminal time point and may not capture shifts in pulmonary pressures or transient interstitial edema that occurs during physiological stress[177]. More sensitive or complementary methods include measuring pulmonary capillary wedge pressure under stress, Doppler-based assessment of pulmonary venous flow or tricuspid regurgitation velocity, lung ultrasound, or high-resolution micro-CT imaging to evaluate interstitial fluid accumulation[176–178]. Because this study assessed pulmonary congestion only at rest and using a terminal wet-to-dry measurement, the absence of differences between groups does not rule out the possibility of pulmonary congestion in this model.

Inflammatory characterization was also limited. Only F4/80^{+} macrophages were quantified, and the small sample size restricts the strength of conclusions regarding inflammatory activation. These observations are based on preliminary findings and a limited set of markers, so they should be interpreted cautiously until confirmed with expanded inflammatory profiling. Although co-staining with CCR2 was attempted to distinguish recruited monocyte-derived

macrophages from resident populations, the staining was unsuccessful and will require troubleshooting in future experiments. No additional inflammatory markers, macrophage subtypes, or co-staining approaches were included. TNFα expression, which is central to the second hypothesis, was not directly measured. As a result, the specific inflammatory pathways contributing to the chamber specific remodeling observed in this model cannot yet be defined.

Sample size represents an important limitation of this study. Several measurements, particularly the glucose tolerance test, were performed with relatively small n values, which reduces statistical power and limits the strength of these conclusions. In addition, animals in this study reached the terminal time point at different intervention durations ranging from 12 to 18 weeks. The HFpEF phenotype was already apparent by approximately 12 weeks, and extending the intervention to 18 weeks did not meaningfully alter the terminal measurements. For the purpose of characterizing the model, terminal data from all cohorts were therefore combined. Although this approach was appropriate given the stability of the phenotype, it does limit the ability to determine whether more subtle time-dependent differences emerged within this 12-to-18-week range, since terminal structural, functional, electrophysiological, and inflammatory measures were analyzed as a pooled dataset. I am currently performing a sub-analysis of the different intervention durations (12, 15, 17, and 18 weeks) to determine whether the length of exposure influences the severity of the phenotype.

Another important limitation is that only male mice were included in the analyses presented in this thesis. HFpEF is more prevalent in women, and sex is known to influence susceptibility, remodeling patterns, and overall disease presentation in both clinical and experimental settings[179]. A small number of female CD1 cohorts were run, but these animals were not included in the present thesis. In those cohorts, female mice displayed relative protection from developing the HFpEF phenotype under the same intervention, which is consistent with studies showing that female rodents often exhibit attenuated metabolic and hypertensive responses to high-fat feeding and L-NAME administration[180]. Future work will need to incorporate both sexes to more accurately capture sex-specific responses in this model.

4.5.2 Future Directions

Future studies will need to build on these findings by refining the model and expanding several areas of assessment that were beyond the scope of this project. Although the intervention produced many features consistent with HFpEF, the overall phenotype was modest, and several measurements showed trends rather than clear differences. Adjusting specific components of the intervention, such as modifying sucrose concentration, altering the L-NAME dose, or changing the duration of the intervention, may help strengthen the phenotype further without compromising animal health. Another important direction will be to evaluate whether adding an additional pathological hit, such as inducing aortic regurgitation or another form of pressure or volume overload, could intensify the HFpEF phenotype and make it more clinically relevant. A major next step will also be to incorporate stress-based assessments, since HFpEF abnormalities often become unmasked under physiological demand. Approaches such as dobutamine challenge during invasive pressure recordings or echocardiography would help determine whether the model exhibits impaired diastolic reserve, which is a defining feature of HFpEF.

Pulmonary congestion will also need to be evaluated with more sensitive methods. Resting wet-to-dry lung weights did not show differences, but congestion in HFpEF typically emerges during stress rather than at baseline. Techniques such as stress hemodynamics, Doppler-based assessment of pulmonary venous flow, or imaging methods like micro-CT or lung ultrasound may provide a clearer picture of pulmonary involvement in future work[175,177,178]. In addition, future studies should include direct assessment of diastolic dysfunction using tissue Doppler imaging, since this method is widely used in both clinical and preclinical HFpEF research to detect impaired relaxation and elevated filling pressures[2]. Incorporating tissue Doppler, along with invasive haemodynamic recordings, would allow a more complete characterization of diastolic function and help determine whether the model exhibits the impaired filling patterns that define HFpEF.

The inflammatory findings also highlight an important direction moving forward. The current study used F4/80 staining alone, and although it revealed increased macrophage density in both chambers, a more complete inflammatory profile will be necessary. Future experiments should include additional markers to distinguish macrophage subtypes, assess recruitment pathways, and should also incorporate flow cytometry to more accurately quantify macrophage subpopulations and confirm whether changes in immune cell composition are contributing to the

remodeling patterns seen in this model. Direct measurement of TNFα and its downstream signaling will be especially important given the central hypothesis of this thesis. Once the model is fully stabilized, using pharmacological TNFα inhibition or TNFα gene deletion models will help determine how this cytokine contributes to atrial and ventricular remodeling.

Increasing sample sizes for certain analyses, particularly the glucose tolerance test, will strengthen conclusions about metabolic function. It will also be important to include sex as a biological variable in future cohorts. Although female CD1 mice were not formally included in this thesis, preliminary work from a small number of female cohorts suggested that they were relatively protected from developing the HFpEF phenotype under the same intervention, consistent with other studies showing similar findings in other mouse strains[180]. This finding contrasts with clinical observations in humans, where HFpEF is more common in women and sex is known to influence susceptibility[179]. The discrepancy between human data and the apparent protection seen in female mice highlights an important gap in our understanding. Future studies should specifically investigate sex-based differences in this model to determine the basis for protection in female mice.

Finally, future studies would benefit from longitudinal assessments. In this project, terminal measurements were combined across cohorts that completed 12 to 18 weeks of intervention, and while the phenotype appeared by roughly 12 weeks and remained stable thereafter, intermediate time points were not systematically evaluated. Tracking blood pressure, cardiac function, inflammatory markers, and exercise capacity over time would help clarify when specific features of the phenotype first appear and how atrial and ventricular remodeling progress throughout the intervention.

Together, these directions will strengthen the model, improve its clinical relevance, and provide the framework needed to directly test how TNFα signaling contributes to chamber-specific remodeling in HFpEF.

4.6 Conclusion

Together, this work establishes a refined but modest HFpEF model in CD1 mice and demonstrates that combined metabolic and hypertensive stress produces chamber-specific remodeling with increased atrial vulnerability. Although many features aligned with human

HFpEF, several abnormalities were mild or showed only directional trends, suggesting that the current model captures early or moderate disease rather than a severe phenotype. Nonetheless, the integration of metabolic dysfunction, impaired diastolic filling, concentric remodelling, exercise intolerance, hypertension, and atrial remodelling provides a clinically relevant framework for examining how HFpEF promotes susceptibility to atrial fibrillation and sets the stage for future studies to examine the molecular and cellular pathways that underlie this vulnerability.

Chapter 5: References

1. Tong, D. *et al.* Impaired AMP-Activated Protein Kinase Signaling in Heart Failure with Preserved Ejection Fraction-Associated Atrial Fibrillation. *Circulation* **146**, 73–76 (2022).
2. Roh, J., Hill, J. A., Singh, A., Valero-Muñoz, M. & Sam, F. Heart Failure With Preserved Ejection Fraction: Heterogeneous Syndrome, Diverse Preclinical Models. *Circ Res* **130**, 1906–1925 (2022).
3. Simmonds, S. J., Cuijpers, I., Heymans, S. & Jones, E. A. V. Cellular and Molecular Differences between HFpEF and HFrEF: A Step Ahead in an Improved Pathological Understanding. *Cells* **9**, (2020).
4. Kornej, J., Börschel, C. S., Benjamin, E. J. & Schnabel, R. B. Epidemiology of Atrial Fibrillation in the 21st Century Novel Methods and New Insights. *Circ Res* **127**, 4–20 (2020).
5. Staerk, L., Sherer, J. A., Ko, D., Benjamin, E. J. & Helm, R. H. Atrial Fibrillation: Epidemiology, Pathophysiology, and Clinical Outcomes. *Circ Res* **120**, 1501–1517 (2017).
6. Violi, F., Pastori, D. & Pignatelli, P. Mechanisms And Management Of Thrombo-Embolism In Atrial Fibrillation. **7**, (2014).
7. Benjamin, E. J. *et al.* Independent risk factors for atrial fibrillation in a population-based cohort. The Framingham Heart Study. *JAMA* **271**, 840–4 (1994).
8. Aschar-Sobbi, R. *et al.* Increased atrial arrhythmia susceptibility induced by intense endurance exercise in mice requires TNFα. *Nat Commun* **6**, 6018 (2015).
9. De Jong, A. M. *et al.* Atrial remodeling is directly related to end-diastolic left ventricular pressure in a mouse model of ventricular pressure overload. *PLoS One* **8**, e72651 (2013).
10. Atienza, F., Martins, R. P. & Jalife, J. Translational research in atrial fibrillation: a quest for mechanistically based diagnosis and therapy. *Circ Arrhythm Electrophysiol* **5**, 1207–15 (2012).
11. Ho, S. Y., Anderson, R. H. & Sánchez-Quintana, D. Atrial structure and fibres: morphologic bases of atrial conduction. *Cardiovasc Res* **54**, 325–36 (2002).
12. Spencer, K. T. *et al.* Effects of aging on left atrial reservoir, conduit, and booster pump function: a multi-institution acoustic quantification study. *Heart* **85**, 272–7 (2001).
13. Goette, A. *et al.* EHRA/HRS/APHRS/SOLAECE expert consensus on atrial cardiomyopathies: Definition, characterization, and clinical implication. *Heart Rhythm* **14**, e3–e40 (2017).
14. Bers, D. M. Cardiac excitation-contraction coupling. *Nature* **415**, 198–205 (2002).
15. Bhattacharyya, S. & Munshi, N. V. Development of the Cardiac Conduction System. *Cold Spring Harb Perspect Biol* **12**, (2020).
16. Han, B., Trew, M. L. & Zgierski-Johnston, C. M. Cardiac Conduction Velocity, Remodeling and Arrhythmogenesis. *Cells* **10**, (2021).
17. Blatter, L. A., Kanaporis, G., Martinez-Hernandez, E., Oropeza-Almazan, Y. & Banach, K. Excitation-contraction coupling and calcium release in atrial muscle. *Pflugers Arch* **473**, 317–329 (2021).
18. Eisner, D. A., Caldwell, J. L., Kistamás, K. & Trafford, A. W. Calcium and Excitation-Contraction Coupling in the Heart. *Circ Res* **121**, 181–195 (2017).

19. King, J. H., Huang, C. L.-H. & Fraser, J. A. Determinants of myocardial conduction velocity: implications for arrhythmogenesis. *Front Physiol* **4**, 154 (2013).
20. Spector, P. Principles of cardiac electric propagation and their implications for re-entrant arrhythmias. *Circ Arrhythm Electrophysiol* **6**, 655–61 (2013).
21. Filgueiras-Rama, D. & Jalife, J. STRUCTURAL AND FUNCTIONAL BASES OF CARDIAC FIBRILLATION. DIFFERENCES AND SIMILARITIES BETWEEN ATRIA AND VENTRICLES. *JACC Clin Electrophysiol* **2**, 1–3 (2016).
22. Augustin, C. M. *et al.* The impact of wall thickness and curvature on wall stress in patient-specific electromechanical models of the left atrium. *Biomech Model Mechanobiol* **19**, 1015–1034 (2020).
23. Grandi, E. *et al.* Human atrial action potential and Ca2+ model: sinus rhythm and chronic atrial fibrillation. *Circ Res* **109**, 1055–66 (2011).
24. Amos, G. J. *et al.* Differences between outward currents of human atrial and subepicardial ventricular myocytes. *J Physiol* **491**, 31–50 (1996).
25. Nattel, S., Burstein, B. & Dobrev, D. Atrial remodeling and atrial fibrillation: mechanisms and implications. *Circ Arrhythm Electrophysiol* **1**, 62–73 (2008).
26. Daou, D., Tong, D., Schiattarella, G. G., Gillette, T. G. & Hill, J. A. What is Cardiometabolic HFpEF and How Can We Study it Preclinically? *JACC Basic Transl Sci* 101295 (2025) doi:10.1016/j.jacbts.2025.04.009.
27. McDonagh, T. A. *et al.* 2021 ESC Guidelines for the diagnosis and treatment of acute and chronic heart failure. *Eur Heart J* **42**, 3599–3726 (2021).
28. Heidenreich, P. A. *et al.* 2022 AHA/ACC/HFSA Guideline for the Management of Heart Failure: A Report of the American College of Cardiology/American Heart Association Joint Committee on Clinical Practice Guidelines. *J Am Coll Cardiol* **79**, e263–e421 (2022).
29. Bozkurt, B. *et al.* Universal definition and classification of heart failure: a report of the Heart Failure Society of America, Heart Failure Association of the European Society of Cardiology, Japanese Heart Failure Society and Writing Committee of the Universal Definition of Heart Failure: Endorsed by the Canadian Heart Failure Society, Heart Failure Association of India, Cardiac Society of Australia and New Zealand, and Chinese Heart Failure Association. *Eur J Heart Fail* **23**, 352–380 (2021).
30. Borlaug, B. A. The pathophysiology of heart failure with preserved ejection fraction. *Nat Rev Cardiol* **11**, 507–15 (2014).
31. Kobak, K. A., Zarzycka, W. & Chiao, Y. A. Age and Sex Differences in Heart Failure With Preserved Ejection Fraction. *Frontiers in aging* **3**, 811436 (2022).
32. Gevaert, A. B., Boen, J. R. A., Segers, V. F. & Van Craenenbroeck, E. M. Heart Failure With Preserved Ejection Fraction: A Review of Cardiac and Noncardiac Pathophysiology. *Front Physiol* **10**, 638 (2019).
33. Paulus, W. J. & Tschöpe, C. A novel paradigm for heart failure with preserved ejection fraction: comorbidities drive myocardial dysfunction and remodeling through coronary microvascular endothelial inflammation. *J Am Coll Cardiol* **62**, 263–71 (2013).
34. Wintrich, J. *et al.* Therapeutic approaches in heart failure with preserved ejection fraction: past, present, and future. *Clinical Research in Cardiology* **109**, 1079–1098 (2020).

35. Gordon, A. M., Homsher, E. & Regnier, M. Regulation of contraction in striated muscle. *Physiol Rev* **80**, 853–924 (2000).
36. Jeong, E.-M. & Dudley, S. C. Diastolic dysfunction. *Circ J* **79**, 470–7 (2015).
37. Liu, C.-F. & Tang, W. H. W. Epigenetics in Cardiac Hypertrophy and Heart Failure. *JACC Basic Transl Sci* **4**, 976–993 (2019).
38. Daou, D., Gillette, T. G. & Hill, J. A. Inflammatory Mechanisms in Heart Failure with Preserved Ejection Fraction. *Physiology (Bethesda)* **38**, 0 (2023).
39. Sanders-van Wijk, S. *et al.* Proteomic Evaluation of the Comorbidity-Inflammation Paradigm in Heart Failure With Preserved Ejection Fraction: Results From the PROMIS-HFpEF Study. *Circulation* **142**, 2029–2044 (2020).
40. Aktan, F. iNOS-mediated nitric oxide production and its regulation. *Life Sci* **75**, 639–53 (2004).
41. Jia, J., Liu, Y., Zhang, X., Liu, X. & Qi, J. Regulation of iNOS expression by NF-κB in human lens epithelial cells treated with high levels of glucose. *Invest Ophthalmol Vis Sci* **54**, 5070–7 (2013).
42. Schiattarella, G. G. *et al.* Nitrosative stress drives heart failure with preserved ejection fraction. *Nature 2019 568:7752* **568**, 351–356 (2019).
43. Packer, M. Epicardial Adipose Tissue May Mediate Deleterious Effects of Obesity and Inflammation on the Myocardium. *J Am Coll Cardiol* **71**, 2360–2372 (2018).
44. van Woerden, G. *et al.* Epicardial Adipose Tissue and Outcome in Heart Failure With Mid-Range and Preserved Ejection Fraction. *Circ Heart Fail* **15**, e009238 (2022).
45. Koepp, K. E., Obokata, M., Reddy, Y. N. V., Olson, T. P. & Borlaug, B. A. Hemodynamic and Functional Impact of Epicardial Adipose Tissue in Heart Failure With Preserved Ejection Fraction. *JACC Heart Fail* **8**, 657–666 (2020).
46. Venkateshvaran, A. *et al.* Association of epicardial adipose tissue with proteomics, coronary flow reserve, cardiac structure and function, and quality of life in heart failure with preserved ejection fraction: insights from the PROMIS-HFpEF study. *Eur J Heart Fail* **24**, 2251–2260 (2022).
47. Travers, J. G., Kamal, F. A., Robbins, J., Yutzey, K. E. & Blaxall, B. C. Cardiac Fibrosis: The Fibroblast Awakens. *Circ Res* **118**, 1021–40 (2016).
48. Frangogiannis, N. G. Cardiac fibrosis. *Cardiovasc Res* **117**, 1450–1488 (2021).
49. Schimmel, K., Ichimura, K., Reddy, S., Haddad, F. & Spiekerkoetter, E. Cardiac Fibrosis in the Pressure Overloaded Left and Right Ventricle as a Therapeutic Target. *Front Cardiovasc Med* **9**, 886553 (2022).
50. Weber, K. T. Cardiac interstitium in health and disease: the fibrillar collagen network. *J Am Coll Cardiol* **13**, 1637–52 (1989).
51. Liu, H. *et al.* Dynamic and static biomechanical traits of cardiac fibrosis. *Front Bioeng Biotechnol* **10**, 1042030 (2022).
52. Chute, M., Aujla, P., Jana, S. & Kassiri, Z. The Non-Fibrillar Side of Fibrosis: Contribution of the Basement Membrane, Proteoglycans, and Glycoproteins to Myocardial Fibrosis. *J Cardiovasc Dev Dis* **6**, (2019).
53. Silva, A. C., Pereira, C., Fonseca, A. C. R. G., Pinto-do-Ó, P. & Nascimento, D. S. Bearing My Heart: The Role of Extracellular Matrix on Cardiac Development, Homeostasis, and Injury Response. *Front Cell Dev Biol* **8**, 621644 (2020).

54. Ravassa, S. *et al.* Biomarker-based assessment of collagen cross-linking identifies patients at risk of heart failure more likely to benefit from spironolactone effects on left atrial remodelling. Insights from the HOMAGE clinical trial. *Eur J Heart Fail* **24**, 321–331 (2022).
55. Mewton, N., Liu, C. Y., Croisille, P., Bluemke, D. & Lima, J. A. C. Assessment of myocardial fibrosis with cardiovascular magnetic resonance. *J Am Coll Cardiol* **57**, 891–903 (2011).
56. Kasner, M. *et al.* Diastolic tissue Doppler indexes correlate with the degree of collagen expression and cross-linking in heart failure and normal ejection fraction. *J Am Coll Cardiol* **57**, 977–85 (2011).
57. Phan, T. T. *et al.* Heart failure with preserved ejection fraction is characterized by dynamic impairment of active relaxation and contraction of the left ventricle on exercise and associated with myocardial energy deficiency. *J Am Coll Cardiol* **54**, 402–9 (2009).
58. Hahn, V. S. *et al.* Myocardial Metabolomics of Human Heart Failure With Preserved Ejection Fraction. *Circulation* **147**, 1147–1161 (2023).
59. Riehle, C. & Abel, E. D. Insulin Signaling and Heart Failure. *Circ Res* **118**, 1151–69 (2016).
60. Duncan, R. E., Ahmadian, M., Jaworski, K., Sarkadi-Nagy, E. & Sul, H. S. Regulation of lipolysis in adipocytes. *Annu Rev Nutr* **27**, 79–101 (2007).
61. Boden, G. Obesity, insulin resistance and free fatty acids. *Curr Opin Endocrinol Diabetes Obes* **18**, 139–43 (2011).
62. Leggat, J., Bidault, G. & Vidal-Puig, A. Lipotoxicity: a driver of heart failure with preserved ejection fraction? *Clin Sci (Lond)* **135**, 2265–2283 (2021).
63. Sun, Q., Karwi, Q. G., Wong, N. & Lopaschuk, G. D. Advances in myocardial energy metabolism: metabolic remodelling in heart failure and beyond. *Cardiovasc Res* **120**, 1996–2016 (2024).
64. Sharma, N. *et al.* High-sugar diets increase cardiac dysfunction and mortality in hypertension compared to low-carbohydrate or high-starch diets. *J Hypertens* **26**, 1402–10 (2008).
65. Zibadi, S., Vazquez, R., Moore, D., Larson, D. F. & Watson, R. R. Myocardial lysyl oxidase regulation of cardiac remodeling in a murine model of diet-induced metabolic syndrome. *Am J Physiol Heart Circ Physiol* **297**, H976-82 (2009).
66. Gao, S. *et al.* Animal models of heart failure with preserved ejection fraction (HFpEF): from metabolic pathobiology to drug discovery. *Acta Pharmacol Sin* **45**, 23–35 (2024).
67. Wang, C.-Y. & Liao, J. K. A mouse model of diet-induced obesity and insulin resistance. *Methods Mol Biol* **821**, 421–33 (2012).
68. Yaspelkis, B. B., Kvasha, I. A. & Figueroa, T. Y. High-fat feeding increases insulin receptor and IRS-1 coimmunoprecipitation with SOCS-3, IKKalpha/beta phosphorylation and decreases PI-3 kinase activity in muscle. *Am J Physiol Regul Integr Comp Physiol* **296**, R1709-15 (2009).
69. Arkan, M. C. *et al.* IKK-β links inflammation to obesity-induced insulin resistance. *Nat Med* **11**, 191–198 (2005).
70. Copps, K. D. & White, M. F. Regulation of insulin sensitivity by serine/threonine phosphorylation of insulin receptor substrate proteins IRS1 and IRS2. *Diabetologia* **55**, 2565–2582 (2012).
71. Wright, J. J. *et al.* Mechanisms for increased myocardial fatty acid utilization following short-term high-fat feeding. *Cardiovasc Res* **82**, 351–60 (2009).

72. Khalid, M., Alkaabi, J., Khan, M. A. B. & Adem, A. Insulin Signal Transduction Perturbations in Insulin Resistance. *Int J Mol Sci* **22**, (2021).
73. Lopaschuk, G. D., Ussher, J. R., Folmes, C. D. L., Jaswal, J. S. & Stanley, W. C. Myocardial fatty acid metabolism in health and disease. *Physiol Rev* **90**, 207–58 (2010).
74. Shoelson, S. E., Lee, J. & Goldfine, A. B. Inflammation and insulin resistance. *J Clin Invest* **116**, 1793–801 (2006).
75. Drosatos, K. & Schulze, P. C. Cardiac lipotoxicity: molecular pathways and therapeutic implications. *Curr Heart Fail Rep* **10**, 109–21 (2013).
76. Sletten, A. C., Peterson, L. R. & Schaffer, J. E. Manifestations and mechanisms of myocardial lipotoxicity in obesity. *J Intern Med* **284**, 478–491 (2018).
77. Natarajan, N. *et al.* Effect of dietary fat and sucrose consumption on cardiac fibrosis in mice and rhesus monkeys. *JCI Insight* **4**, (2019).
78. Huneault, H. E., Ramirez Tovar, A., Sanchez-Torres, C., Welsh, J. A. & Vos, M. B. The Impact and Burden of Dietary Sugars on the Liver. *Hepatol Commun* **7**, (2023).
79. Dong, S. *et al.* Changes of myocardial lipidomics profiling in a rat model of diabetic cardiomyopathy using UPLC/Q-TOF/MS analysis. *Diabetol Metab Syndr* **9**, 56 (2017).
80. Sverdlov, A. L. *et al.* High fat, high sucrose diet causes cardiac mitochondrial dysfunction due in part to oxidative post-translational modification of mitochondrial complex II. *J Mol Cell Cardiol* **78**, 165–73 (2015).
81. Qin, F. *et al.* Hydrogen peroxide-mediated SERCA cysteine 674 oxidation contributes to impaired cardiac myocyte relaxation in senescent mouse heart. *J Am Heart Assoc* **2**, e000184 (2013).
82. Giacco, F. & Brownlee, M. Oxidative stress and diabetic complications. *Circ Res* **107**, 1058–70 (2010).
83. Triggle, C. R. & Ding, H. A review of endothelial dysfunction in diabetes: a focus on the contribution of a dysfunctional eNOS. *J Am Soc Hypertens* **4**, 102–15 (2010).
84. Funk, S. D., Yurdagul, A. & Orr, A. W. Hyperglycemia and endothelial dysfunction in atherosclerosis: lessons from type 1 diabetes. *Int J Vasc Med* **2012**, 569654 (2012).
85. Candido, R. *et al.* A Breaker of Advanced Glycation End Products Attenuates Diabetes-Induced Myocardial Structural Changes. *Circ Res* **92**, 785–792 (2003).
86. Gao, X., Zhang, H., Schmidt, A. M. & Zhang, C. AGE/RAGE produces endothelial dysfunction in coronary arterioles in Type 2 diabetic mice. *American Journal of Physiology-Heart and Circulatory Physiology* **295**, H491–H498 (2008).
87. Alderton, W. K., COOPER, C. E. & KNOWLES, R. G. Nitric oxide synthases: structure, function and inhibition. *Biochemical Journal* **357**, 593 (2001).
88. Forstermann, U. & Sessa, W. C. Nitric oxide synthases: regulation and function. *Eur Heart J* **33**, 829–837 (2012).
89. Cai, Z. *et al.* The NO-cGMP-PKG Axis in HFpEF: From Pathological Mechanisms to Potential Therapies. *Aging Dis* **14**, 46–62 (2023).
90. Pechanova, O., Vrankova, S. & Cebova, M. Chronic L-Name-Treatment Produces Hypertension by Different Mechanisms in Peripheral Tissues and Brain: Role of Central eNOS. *Pathophysiology* **27**, 46–54 (2020).

91. Gao, Y. *et al.* Naringenin inhibits NG-nitro-L-arginine methyl ester-induced hypertensive left ventricular hypertrophy by decreasing angiotensin-converting enzyme 1 expression. *Exp Ther Med* **16**, 867–873 (2018).
92. Borbély, A. *et al.* Hypophosphorylation of the Stiff N2B Titin Isoform Raises Cardiomyocyte Resting Tension in Failing Human Myocardium. *Circ Res* **104**, 780–786 (2009).
93. Tschöpe, C. & Van Linthout, S. New insights in (inter)cellular mechanisms by heart failure with preserved ejection fraction. *Curr Heart Fail Rep* **11**, 436–44 (2014).
94. Glezeva, N. & Baugh, J. A. Role of inflammation in the pathogenesis of heart failure with preserved ejection fraction and its potential as a therapeutic target. *Heart Fail Rev* **19**, 681–694 (2014).
95. Cohn, J. N., Ferrari, R. & Sharpe, N. Cardiac remodeling--concepts and clinical implications: a consensus paper from an international forum on cardiac remodeling. Behalf of an International Forum on Cardiac Remodeling. *J Am Coll Cardiol* **35**, 569–82 (2000).
96. Aronow, W. S. Hypertension and left ventricular hypertrophy. *Ann Transl Med* **5**, 310 (2017).
97. Nakamura, M. & Sadoshima, J. Mechanisms of physiological and pathological cardiac hypertrophy. *Nat Rev Cardiol* **15**, 387–407 (2018).
98. Grossman, W., Jones, D. & McLaurin, L. P. Wall stress and patterns of hypertrophy in the human left ventricle. *Journal of Clinical Investigation* **56**, 56–64 (1975).
99. Heineke, J. & Molkentin, J. D. Regulation of cardiac hypertrophy by intracellular signalling pathways. *Nat Rev Mol Cell Biol* **7**, 589–600 (2006).
100. Kong, P., Christia, P. & Frangogiannis, N. G. The pathogenesis of cardiac fibrosis. *Cell Mol Life Sci* **71**, 549–74 (2014).
101. Strait, J. B. & Lakatta, E. G. Aging-associated cardiovascular changes and their relationship to heart failure. *Heart Fail Clin* **8**, 143–64 (2012).
102. Lakatta, E. G. & Levy, D. Arterial and cardiac aging: major shareholders in cardiovascular disease enterprises: Part I: aging arteries: a 'set up' for vascular disease. *Circulation* **107**, 139–46 (2003).
103. Steenman, M. & Lande, G. Cardiac aging and heart disease in humans. *Biophys Rev* **9**, 131–137 (2017).
104. Zile, M. R., Baicu, C. F. & Gaasch, W. H. Diastolic heart failure--abnormalities in active relaxation and passive stiffness of the left ventricle. *N Engl J Med* **350**, 1953–9 (2004).
105. Golla, M. S. G. & Shams, P. *Heart Failure With Preserved Ejection Fraction (HFpEF)*. (2025).
106. Haykal, R., Kassar, A., Chamoun, N. & Akoum, N. The left atrium in heart failure with preserved ejection fraction: What we know and what we do not know. *Heart Rhythm O2* **6**, 1028–1038 (2025).
107. Peigh, G., Shah, S. J. & Patel, R. B. Left Atrial Myopathy in Atrial Fibrillation and Heart Failure: Clinical Implications, Mechanisms, and Therapeutic Targets. *Curr Heart Fail Rep* **18**, 85–98 (2021).
108. Ariyaratnam, J. P. *et al.* Heart failure with preserved ejection fraction: An alternative paradigm to explain the clinical implications of atrial fibrillation. *Heart Rhythm O2* **2**, 771–783 (2021).

109. Zain, S., Shamshad, T., Kabir, A. & Khan, A. A. Epicardial Adipose Tissue and Development of Atrial Fibrillation (AFIB) and Heart Failure With Preserved Ejection Fraction (HFpEF). *Cureus* https://doi.org/10.7759/cureus.46153 (2023) doi:10.7759/cureus.46153.
110. Melenovsky, V. *et al.* Left Atrial Remodeling and Function in Advanced Heart Failure With Preserved or Reduced Ejection Fraction. *Circ Heart Fail* **8**, 295–303 (2015).
111. Telles, F. *et al.* Impaired left atrial strain predicts abnormal exercise haemodynamics in heart failure with preserved ejection fraction. *Eur J Heart Fail* **21**, 495–505 (2019).
112. Santos, A. B. S. *et al.* Prognostic Relevance of Left Atrial Dysfunction in Heart Failure With Preserved Ejection Fraction. *Circ Heart Fail* **9**, (2016).
113. Paulus, W. J. & Zile, M. R. From Systemic Inflammation to Myocardial Fibrosis: The Heart Failure With Preserved Ejection Fraction Paradigm Revisited. *Circ Res* **128**, 1451–1467 (2021).
114. Kim, D. & Baek, J.-H. Macrophages and fibroblasts in cardiac fibrosis: interactions and transformation. *Exploration of Immunology* **5**, (2025).
115. Murphy, S. P., Kakkar, R., McCarthy, C. P. & Januzzi, J. L. Inflammation in Heart Failure. *J Am Coll Cardiol* **75**, 1324–1340 (2020).
116. Yerra, V. G. & Advani, A. Role of CCR2-Positive Macrophages in Pathological Ventricular Remodelling. *Biomedicines* **10**, 661 (2022).
117. Zeisberg, E. M. *et al.* Endothelial-to-mesenchymal transition contributes to cardiac fibrosis. *Nat Med* **13**, 952–961 (2007).
118. Gorter, T. M. *et al.* Epicardial Adipose Tissue and Invasive Hemodynamics in Heart Failure With Preserved Ejection Fraction. *JACC Heart Fail* **8**, 667–676 (2020).
119. Hatem, S. N. & Sanders, P. Epicardial adipose tissue and atrial fibrillation. *Cardiovasc Res* **102**, 205–13 (2014).
120. Meulendijks, E. R. *et al.* Atrial epicardial adipose tissue abundantly secretes myeloperoxidase and activates atrial fibroblasts in patients with atrial fibrillation. *J Transl Med* **21**, 366 (2023).
121. Conte, M. *et al.* Epicardial Adipose Tissue and Cardiac Arrhythmias: Focus on Atrial Fibrillation. *Front Cardiovasc Med* **9**, (2022).
122. De Jong, A. M. *et al.* Mechanisms of atrial structural changes caused by stretch occurring before and during early atrial fibrillation. *Cardiovasc Res* **89**, 754–65 (2011).
123. Weber, K. T. From Inflammation to Fibrosis: A Stiff Stretch of Highway. https://doi.org/10.1161/01.HYP.0000118586.38323.5b (2004) doi:10.1161/01.HYP.0000118586.38323.5b.
124. Iwasaki, Y. K., Nishida, K., Kato, T. & Nattel, S. Atrial fibrillation pathophysiology: Implications for management. *Circulation* **124**, 2264–2274 (2011).
125. Mahajan, R. *et al.* Electrophysiological, Electroanatomical, and Structural Remodeling of the Atria as Consequences of Sustained Obesity. *J Am Coll Cardiol* **66**, 1–11 (2015).
126. Samanta, R., Pouliopoulos, J., Thiagalingam, A. & Kovoor, P. Role of adipose tissue in the pathogenesis of cardiac arrhythmias. *Heart Rhythm* **13**, 311–320 (2016).
127. Ernault, A. C., Meijborg, V. M. F. & Coronel, R. Modulation of Cardiac Arrhythmogenesis by Epicardial Adipose Tissue. *J Am Coll Cardiol* **78**, 1730–1745 (2021).

128. Jacquemet, V., Virag, N. & Kappenberger, L. Wavelength and vulnerability to atrial fibrillation: Insights from a computer model of human atria. https://doi.org/10.1016/j.eupc.2005.03.017 (2005) doi:10.1016/j.eupc.2005.03.017.
129. Daoud, E. G. *et al.* Effect of atrial fibrillation on atrial refractoriness in humans. *Circulation* **94**, 1600–1606 (1996).
130. Kim, Y. M. *et al.* Apelin increases atrial conduction velocity, refractoriness, and prevents inducibility of atrial fibrillation. https://doi.org/10.1172/jci.insight.126525 (2020) doi:10.1172/jci.insight.126525.
131. Burstein, B. *et al.* Changes in connexin expression and the atrial fibrillation substrate in congestive heart failure. *Circ Res* **105**, 1213–1222 (2009).
132. Guo, Y.-H. & Yang, Y.-Q. Atrial Fibrillation: Focus on Myocardial Connexins and Gap Junctions. *Biology (Basel)* **11**, (2022).
133. Zhang, F., Hartnett, S., Sample, A., Schnack, S. & Li, Y. High fat diet induced alterations of atrial electrical activities in mice. *Am J Cardiovasc Dis* **6**, 1–9 (2016).
134. McCully, B. H. *et al.* Sympathetic cardiac hyperinnervation and atrial autonomic imbalance in diet-induced obesity promote cardiac arrhythmias. *Am J Physiol Heart Circ Physiol* **305**, H1530-7 (2013).
135. Solaro, N., Pagani, M. & Lucini, D. Altered Cardiac Autonomic Regulation in Overweight and Obese Subjects: The Role of Age-and-Gender-Adjusted Statistical Indicators of Heart Rate Variability and Cardiac Baroreflex. *Front Physiol* **11**, 567312 (2020).
136. Takahashi, K. *et al.* High-fat diet increases vulnerability to atrial arrhythmia by conduction disturbance via miR-27b. https://doi.org/10.1016/j.yjmcc.2015.11.034 (2015) doi:10.1016/j.yjmcc.2015.11.034.
137. Walfridsson, H. *et al.* Is the acetylcholine-regulated inwardly rectifying potassium current a viable antiarrhythmic target? Translational discrepancies of AZD2927 and A7071 in dogs and humans. *Europace* **17**, 473–482 (2015).
138. Nattel, S. & Dobrev, D. Role of Calcium-activated Potassium Channels in Atrial Fibrillation Pathophysiology and Therapy. *Journal of Cardiovasular Pharmacology* **66**, 5–409 (2015).
139. Li, N. *et al.* Ablation of a Ca 2+-activated K + channel (SK2 channel) results in action potential prolongation in atrial myocytes and atrial fibrillation. *J Physiol* **587**, 1087–1100 (2009).
140. Levine, B., Kalman, J., Mayer, L., Fillit, H. M. & Packer, M. Elevated Circulating Levels of Tumor Necrosis Factor in Severe Chronic Heart Failure. *New England Journal of Medicine* **323**, 236–241 (1990).
141. McMurray, J., Abdullah, I., Dargie, H. J. & Shapiro, D. Increased concentrations of tumour necrosis factor in 'cachectic' patients with severe chronic heart failure. *Br Heart J* **66**, 356–8 (1991).
142. Mann, D. L. *et al.* Targeted anticytokine therapy in patients with chronic heart failure: results of the Randomized Etanercept Worldwide Evaluation (RENEWAL). *Circulation* **109**, 1594–1602 (2004).
143. Kroetsch, J. T. & Bolz, S. S. The TNF-α/Sphingosine-1-Phosphate Signaling Axis Drives Myogenic Responsiveness in Heart Failure. *J Vasc Res* **50**, 177–185 (2013).

144. Kroetsch, J. T. *et al.* Constitutive smooth muscle tumour necrosis factor regulates microvascular myogenic responsiveness and systemic blood pressure. *Nat Commun* **8**, 14805 (2017).
145. Mann, D. L. & Young, J. B. Basic Mechanisms in Congestive Heart Failure: Recognizing the Role of Proinflammatory Cytokines. *Chest* **105**, 897–904 (1994).
146. Schumacher, S. M. & Naga Prasad, S. V. Tumor Necrosis Factor-α in Heart Failure: an Updated Review. *Curr Cardiol Rep* **20**, 117 (2018).
147. Zhou, X. & Dudley, S. C. Evidence for Inflammation as a Driver of Atrial Fibrillation. *Front Cardiovasc Med* **7**, (2020).
148. Korantzopoulos, P. *et al.* Inflammation and atrial fibrillation: A comprehensive review. *J Arrhythm* **34**, 394–401 (2018).
149. Chung, E. S., Packer, M., Lo, K. H., Fasanmade, A. A. & Willerson, J. T. Randomized, Double-Blind, Placebo-Controlled, Pilot Trial of Infliximab, a Chimeric Monoclonal Antibody to Tumor Necrosis Factor-α, in Patients With Moderate-to-Severe Heart Failure. *Circulation* **107**, 3133–3140 (2003).
150. Beyfuss, K., Erlich, A. T., Triolo, M. & Hood, D. A. The Role of p53 in Determining Mitochondrial Adaptations to Endurance Training in Skeletal Muscle. *Sci Rep* **8**, 14710 (2018).
151. Lakin, R. *et al.* Changes in Heart Rate and Its Regulation by the Autonomic Nervous System Do Not Differ Between Forced and Voluntary Exercise in Mice. *Front Physiol* **9**, (2018).
152. Benedé-Ubieto, R., Estévez-Vázquez, O., Ramadori, P., Cubero, F. J. & Nevzorova, Y. A. Guidelines and Considerations for Metabolic Tolerance Tests in Mice</p>. *Diabetes Metab Syndr Obes* **Volume 13**, 439–450 (2020).
153. Gorman, R. A. *et al.* The effects of daily dose of intense exercise on cardiac responses and atrial fibrillation. *J Physiol* **602**, 569–596 (2024).
154. Chess, D. J., Lei, B., Hoit, B. D., Azimzadeh, A. M. & Stanley, W. C. Deleterious effects of sugar and protective effects of starch on cardiac remodeling, contractile dysfunction, and mortality in response to pressure overload. *Am J Physiol Heart Circ Physiol* **293**, (2007).
155. Gutiérrez, D. *et al.* Early Changes in Cardiac Macrophage Subsets in Heart Failure with Preserved Ejection Fraction. *Int J Mol Sci* **26**, 10196 (2025).
156. Hulsmans, M. *et al.* Cardiac macrophages promote diastolic dysfunction. *Journal of Experimental Medicine* **215**, 423–440 (2018).
157. Fengler, V. H. I. *et al.* Susceptibility of Different Mouse Wild Type Strains to Develop Diet-Induced NAFLD/AFLD-Associated Liver Disease. *PLoS One* **11**, e0155163 (2016).
158. Burchfield, J. G. *et al.* High dietary fat and sucrose result in an extensive and time-dependent deterioration in health of multiple physiological systems in mice. *Journal of Biological Chemistry* **293**, 5731–5745 (2018).
159. Nayor, M. *et al.* Impaired Exercise Tolerance in Heart Failure With Preserved Ejection Fraction. *JACC Heart Fail* **8**, 605–617 (2020).
160. Zern, E. K. *et al.* Exercise Intolerance in Heart Failure With Preserved Ejection Fraction: Arterial Stiffness and Abnormal Left Ventricular Hemodynamic Responses During Exercise. *J Card Fail* **27**, 625–634 (2021).
161. Oh, G. C. & Cho, H.-J. Blood pressure and heart failure. *Clin Hypertens* **26**, 1 (2020).

162. Hashem, M.-S. *et al.* Left Ventricular Relative Wall Thickness Versus Left Ventricular Mass Index in Non-Cardioembolic Stroke Patients. *Medicine* **94**, e872 (2015).
163. Gaasch, W. H. & Zile, M. R. Left Ventricular Structural Remodeling in Health and Disease. *J Am Coll Cardiol* **58**, 1733–1740 (2011).
164. Villalba-Orero, M., Garcia-Pavia, P. & Lara-Pezzi, E. Non-invasive assessment of HFpEF in mouse models: current gaps and future directions. *BMC Med* **20**, 349 (2022).
165. Navarro-Garcia, J. A., Lahiri, S. K., Aguilar-Sanchez, Y., Reddy, A. K. & Wehrens, X. H. T. Characterization of atrial and ventricular remodeling in an improved minimally invasive mouse model of transverse aortic constriction. *The Journal of Cardiovascular Aging* **3**, 31 (2023).
166. Zhang, Y. *et al.* Inhibition of endoplasmic reticulum stress prevents high-fat diet mediated atrial fibrosis and fibrillation. *J Cell Mol Med* **24**, 13660–13668 (2020).
167. Verheule, S. *et al.* Increased Vulnerability to Atrial Fibrillation in Transgenic Mice With Selective Atrial Fibrosis Caused by Overexpression of TGF-β1.
168. Santhanakrishnan, R. *et al.* Atrial Fibrillation Begets Heart Failure and Vice Versa. *Circulation* **133**, 484–492 (2016).
169. Mouton, A. J., Li, X., Hall, M. E. & Hall, J. E. Obesity, Hypertension, and Cardiac Dysfunction. *Circ Res* **126**, 789–806 (2020).
170. Lafuse, W. P., Wozniak, D. J. & Rajaram, M. V. S. Role of Cardiac Macrophages on Cardiac Inflammation, Fibrosis and Tissue Repair. *Cells* **10**, 51 (2020).
171. Lim, G. B. Macrophages promote cardiac fibrosis and diastolic dysfunction. *Nat Rev Cardiol* **15**, 196–197 (2018).
172. Liu, H. *et al.* Inflammatory Macrophage Interleukin-1β Mediates High-Fat Diet-Induced Heart Failure With Preserved Ejection Fraction. *JACC Basic Transl Sci* **8**, 174–185 (2023).
173. Sun, Z. *et al.* Cross-talk between macrophages and atrial myocytes in atrial fibrillation. *Basic Res Cardiol* **111**, 63 (2016).
174. Cho, J. H. Sudden Death and Ventricular Arrhythmias in Heart Failure With Preserved Ejection Fraction. *Korean Circ J* **52**, 251 (2022).
175. Girerd, N. *et al.* Integrative Assessment of Congestion in Heart Failure Throughout the Patient Journey. *JACC Heart Fail* **6**, 273–285 (2018).
176. Pirrotta, F., Mazza, B., Gennari, L. & Palazzuoli, A. Pulmonary Congestion Assessment in Heart Failure: Traditional and New Tools. *Diagnostics* **11**, 1306 (2021).
177. Reddy, Y. N. V *et al.* The haemodynamic basis of lung congestion during exercise in heart failure with preserved ejection fraction. *Eur Heart J* **40**, 3721–3730 (2019).
178. Lindow, T., Quadrelli, S. & Ugander, M. Noninvasive Imaging Methods for Quantification of Pulmonary Edema and Congestion. *JACC Cardiovasc Imaging* **16**, 1469–1484 (2023).
179. Beale, A. L. *et al.* Sex Differences in Heart Failure With Preserved Ejection Fraction Pathophysiology. *JACC Heart Fail* **7**, 239–249 (2019).
180. Tong, D. *et al.* Female Sex Is Protective in a Preclinical Model of Heart Failure With Preserved Ejection Fraction. *Circulation* **140**, 1769–1771 (2019).

Chapter 6: Appendix

A.1 Composition of High fat diet from Research Diets (D12429).

Class description	Ingredients	Grams
Protein	Casein, Lactic, 30 Mesh	200.00 g
Protein	Cystine, L	3.00 g
Carbohydrate	Lodex 10	125.00 g
Carbohydrate	Sucrose, Fine Granulated	72.80 g
Fiber	Solka Floc, FCC200	50.00 g
Fat	Lard	245.00 g
Fat	Soybean Oil, USP	25.00 g
Mineral	S10026B	50.00 g
Vitamin	Choline Bitartrate	2.00 g
Vitamin	V10001C	1.00 g
Dye	Dye, Blue FD&C #1, Alum. Lake 35-42%	0.05 g
	Total:	773.85 g